Cell Communication and Signaling

RESEARCH

Open Access

In-silico predicted mouse melanopsins with blue spectral shifts deliver efficient subcellular signaling

Dhanushan Wijayaratna[1†], Filippo Sacchetta[2†], Laura Pedraza-González[8], Francesca Fanelli[3], Tomohiro Sugihara[4], Mitsumasa Koyanagi[4,5], Senuri Piyawardana[1], Kiran Ghotra[6], Waruna Thotamune[1], Akihisa Terakita[4,5], Massimo Olivucci[2,7*] and Ajith Karunarathne[1*]

Abstract

Melanopsin is a photopigment belonging to the G Protein-Coupled Receptor (GPCR) family expressed in a subset of intrinsically photosensitive retinal ganglion cells (ipRGCs) and responsible for a variety of processes. The bistability and, thus, the possibility to function under low retinal availability would make melanopsin a powerful optogenetic tool. Here, we aim to utilize mouse melanopsin to trigger macrophage migration by its subcellular optical activation with localized blue light, while simultaneously imaging the migration with red light. To reduce melanopsin's red light sensitivity, we employ a combination of in silico structure prediction and automated quantum mechanics/molecular mechanics modeling to predict minimally invasive mutations to shift its absorption spectrum towards the shorter wavelength region of the visible spectrum without compromising the signaling efficiency. The results demonstrate that it is possible to achieve melanopsin mutants that resist red light-induced activation but are activated by blue light and display properties indicating preserved bistability. Using the A333T mutant, we show that the blue light-induced subcellular melanopsin activation triggers localized PIP3 generation and macrophage migration, which we imaged using red light, demonstrating the optogenetic utility of minimally engineered melanopsins.

Keywords Melanopsin, Computational modeling, QM/MM, Optogenetics, GPCR

†Dhanushan Wijayaratna and Filippo Sacchetta contributed equally to this work.

*Correspondence:
Massimo Olivucci
olivucci@unisi.it
Ajith Karunarathne
wkarunarathne@slu.edu
[1]Department of Chemistry, Saint Louis University, Saint Louis, MO 63103, USA
[2]Department of Biotechnology, Chemistry and Pharmacy, University of Siena, Siena, Italy
[3]Department of Life Sciences, Dulbecco Telethon Institute, University of Modena and Reggio Emilia, Modena I-41125, Italy
[4]Department of Biology, Osaka Metropolitan University, O 3-3-138 Sugimoto, Sumiyoshi-Ku, Osaka 558-8585, Japan
[5]The OMU Advanced Research Institute for Natural Science and Technology, Osaka Metropolitan University, Osaka, Japan
[6]Department of Biology, Siena Heights University, Adrian, MI 49221, USA
[7]Department of Chemistry and Center for Photochemical Sciences, Bowling Green State University, Bowling Green, OH 43403, USA
[8]Department of Chemistry and Industrial Chemistry, University of Pisa, Pisa, Italy

Introduction

Optogenetics utilizes genetically encoded proteins with embedded light-sensing modules to control cell signaling using light [1–5]. Light-sensitive G-protein-coupled receptors (GPCRs) or opsins and their chimeric variants have been used to control G protein signaling in cells and in vivo [6–10]. In the dark, a conserved *Lys* in the 7th transmembrane (TM) region of opsins form a protonated Schiff base (PSB) with 11-*cis*-retinal (11CR) chromophore. Upon light (photon) reception, 11CR isomerizes to all-*trans*-retinal (ATR) [11, 12], initiating the photocycle. The photocycle is the process that triggers signaling underlying various biological functions, including vision and circadian processes, and resets the opsin for subsequent photon reception. Some opsins, such as rod and cone opsins in the retina, require a continuous 11CR supply to be functional and are called monostable opsins because they can only form a stable complex in the dark with [13–15]. In the inactive dark state of monostable opsins, a negatively charged (i.e. deprotonated) *Glu* counterion residue on the 3rd TM stabilizes the PSB via a salt bridge [14, 15]. Upon light exposure, the PSB proton is transferred to the counterion, resulting in a large conformational change in the opsin, inducing the hydrolysis of the uncharged all-*trans* Schiff base [14–16]. This is the reason that monostable opsins require a new 11CR molecule to reinstate photon sensitivity. Due to this continuous retinal demand, the optogenetic utility of monostable opsins outside the retina is hindered. In contrast, bistable opsins such as squid rhodopsin [17] (SqRh) and Jumping Spider rhodopsin [18] utilize a *Glu* residue on the extracellular loop 2 (ECL2) above the retinal-binding pocket as a counterion connected to the chromophore PSB via a hydrogen bond network [18]. Since both the 11CR and ATR chromophores are never hydrolyzed during the photocycle, bistable opsins should be able to function under low 11CR concentrations and, therefore, are better candidates for controlling signaling in heterologous cells and in vivo [9].

Most invertebrate opsins are bistable, squid rhodopsin [17] and Jumping Spider rhodopsin [18] are examples. They evolved from the ancestral rhabdomeric photoreceptor cells. However, vertebrates also express bistable opsins such as melanopsin. Melanopsin is expressed primarily in a subset of mammals' intrinsically photosensitive retinal ganglion cells (ipRGCs), and the M1 type ipRGCs, which has the highest melanopsin expression [19, 20], collects the photic information from the retina, and sends it to the suprachiasmatic nucleus (SCN) [21], the master circadian clock [22]. This allows melanopsin to control crucial light-mediated non-image-forming visual functions such as circadian photoentrainment and pupillary light reflexes [19, 23]. Furthermore, studies show that melanopsin signaling affects the mood and behavior of organisms, placing it at the center of several diseases, including seasonal affective disorder, depression, insomnia, and jet lag [24].

Melanopsin has long been recognized as a Gq-coupled photopigment [25, 26]. However, we and others showed that melanopsin efficiently signals through Gq and Gi/o pathways, partly reasoning for its diverse functionality [27, 28]. Melanopsin's ability to activate Gs pathway has also been demonstrated [29]. Although these properties endow melanopsin with great potential as an optogenetic tool to control signaling in cells, its relatively broad, visible region-centered absorption spectrum has made melanopsin sensitive from blue (400 nm) to red wavelengths (up to 600 nm) [27, 30]. Moreover, the long wavelength absorption combined with the high isomerization quantum yields (QY) of ~50% [31] prevents melanopsin's use for controlling the cell behavior while performing, for instance, response imaging [29, 30, 32].

One solution to this problem is to engineer melanopsin variants with the absorption spectrum shifted toward the short wavelength region to make them resist activation by red light [6, 33, 34]. Accordingly, in this study, we search for mouse melanopsin (mMeOp) mutants characterized by an absorption band shifted to shorter wavelengths (see the scheme in Fig. 1a). Such spectral change would allow us to control cellular behavior via blue light while performing response imaging via red light [33, 34] In the past, studies on shifting absorption spectra of opsins through site-directed mutagenesis were conducted to understand the evolution of color vision [35–38]. Several studies have underlined the importance of spectral tuning of opsins during the adaptive evolution of vertebrates and invertebrates, affecting their spectral sensitivity and signaling [39–45]. For instance, *Phe*261 to *Tyr* mutation in freshwater fish rhodopsin makes them more sensitive to red wavelengths compared to other marine species. These alterations in opsins play a crucial role in communication, sexual selection, foraging, and predator avoidance in different aquatic environments [39, 46]. It has been pointed out that *Phe*86*Ala* and *Tyr*93*Asn* mutations in short wavelength-sensitive type 1 (SW1) opsin are strongly associated with violet and ultraviolet sensitivity in mice and American pika [47], contributing to their scotopic-adapted vision and nocturnal activity [48]. Thus, the sequences of red and blue photopigments have been utilized to predict mutations that could shift the opsin absorption spectra [36, 49–51]. However, protein engineering based on comparative structure-spectra analysis and random mutagenesis requires experimentally tedious and inefficient methods of making and testing hundreds of random mutants. Moreover, standard molecular modeling techniques based on molecular mechanics force fields cannot simulate light absorption and, therefore, are unable to assist such engineering efforts.

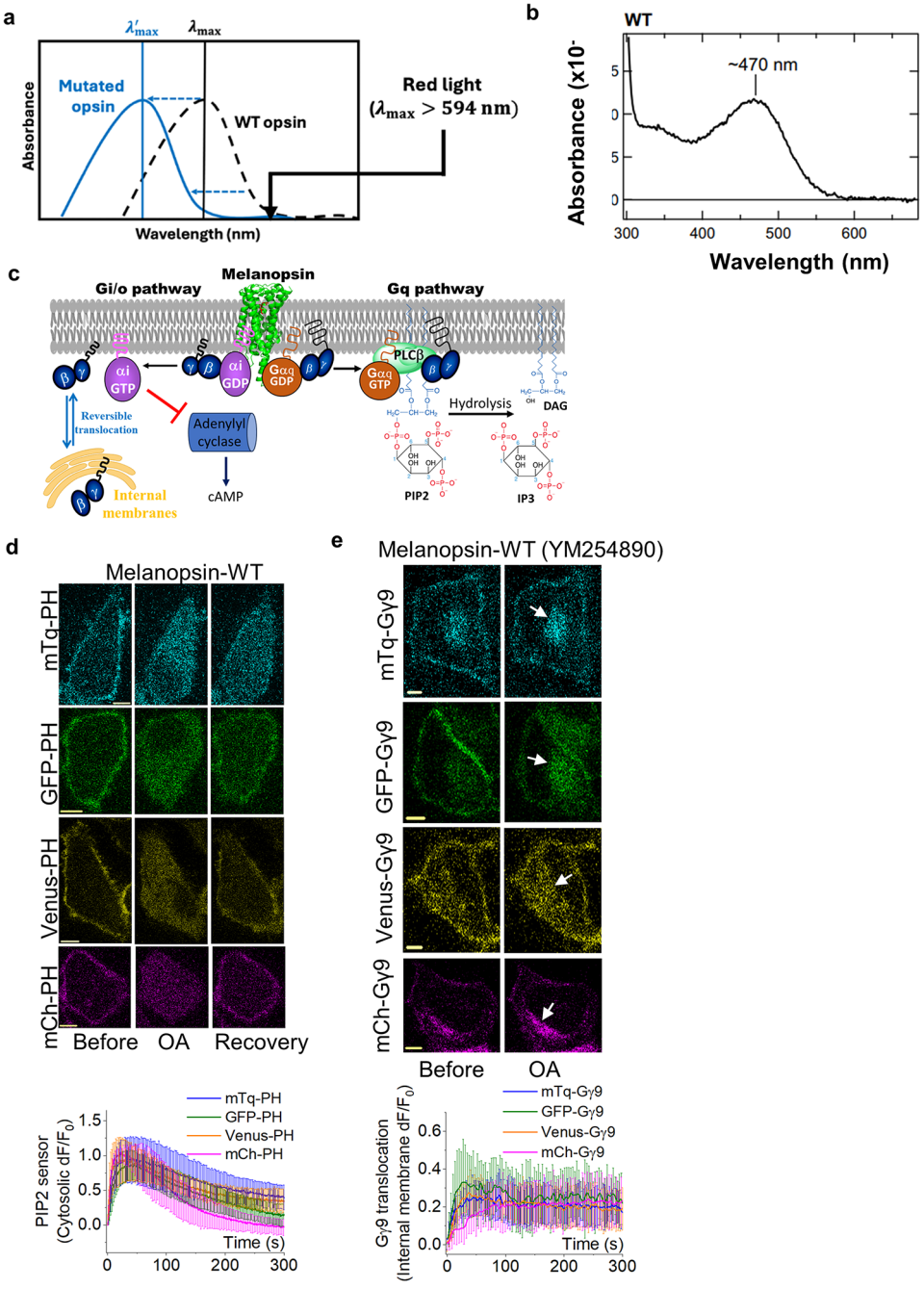

Fig. 1 mMeOp activates both Gq and Gi/o pathways upon sensing the entire visible spectrum. **(a)** Schematic representation of the blue-shift in the absorption maximum (and absorption band) upon mutation (blue full line) of a WT opsin (dashed black line). **(b)** The purified WT-melanopsin photopigment exhibits an absorption maximum (λ^{a}_{max}) of ~470 nm. **(c)** Graphical representation of mMeOp simultaneously activating both Gq and Gi/o pathways, which activate downstream signaling effectors. **(d)** HeLa cells expressing WT mMeOp and PIP2 sensor exhibited robust PIP2 hydrolysis and subsequent recovery upon mMeOp photoactivation by blue (445 nm), green (488 nm), yellow (515 nm), and red (594 nm) colors. Images show the PIP2 sensor tagged with fluorescent proteins of respective colors translocating from the PM to the cytosol upon melanopsin activation. The corresponding plot shows the PIP2 sensor dynamics in the cytosol of the cells in response to different light colors ($n = 48$). **(e)** HeLa cells exhibited robust Gγ9 translocation from the PM to internal membranes (IMs) upon melanopsin activation by blue, green, yellow, and red light in the presence of 500 nM Gq inhibitor (YM-254,890). White arrows indicate the fluorescence intensity increase on IMs due to the Gγ9 translocation. The corresponding plot shows Gγ9 dynamics on the IMs ($n = 46$). Average curves were plotted using 'n' cells, n = number of cells. Error bars represent SD (standard deviation). The scale bar = 5 µm.; WT: wild type; PLC: Phospholipase C; PIP2: phosphatidylinositol 4,5-bisphosphate; PM: Plasma membrane; IMs: Internal membranes; OA: optical activation dF: Fluorescence intensity change; F_0: Fluorescence intensity at time = 0 s

Starting with the seminal work by Warshel [52], the fields of computational photochemistry and photobiology have evolved to include hybrid quantum mechanical/molecular mechanical (QM/MM) calculations. These calculations allow systematic investigations to identify spectral-shifting in wild-type (WT) and mutant opsins in silico [35, 37, 53]. In fact, QM/MM models account for chromophore-protein interactions, including electrostatic and steric effects on the stability of the electronic ground (S_0) and excited state (S_1) of the retinal chromophore [35, 37, 53, 54]. Therefore, they allow for the calculation of spectral properties such as the maximum absorption wavelength (λ^a_{max}); a quantity easily calculated by converting the energy difference between the S_1 and S_0 states into the corresponding wavelength. Such S_1-S_0 energy gap contributes, but does not correspond, to the photoactivation energy (E_a). E_a is defined as the minimum energy required for opsin activation. Many studies have shown that the E_a is not entirely dependent on the feasibility of photon absorption but is also governed by thermal energy [55–58]. It has been predicted that the photon absorbance at higher wavelengths gradually decreases with the portion of molecules with a sufficient complement of thermal energy, where the corresponding E_a is negatively correlated with the wavelength at λ^a_{max} [57, 58]. Thus, the E_a of an opsin is fundamentally related to the λ^a_{max} of the absorbance spectrum and the rate of spontaneous activation. Altogether, these relationships have been comprehensively studied in both invertebrate and vertebrate pigments [55, 59–63]. In the following we will focus on the S_1-S_0 energy gap determining the λ^a_{max} exclusively.

Recently, some of the authors developed a technology called Automatic Rhodopsin Modeling (ARM) for the automated construction of congruent opsin QM/MM models [64] in order to facilitate the construction and utilization of QM/MM models of monostable and bistable opsins and allow for computer-aided opsin engineering. Here, we document how the use of ARM led to the selection ten QM/MM models of mMeOp variants displaying a blue-shifted λ^a_{max} with respect to the WT. We also show how the successive combination of such in silico results with experimental protein engineering and live cell imaging approaches ultimately led to mMeOp mutants that are sufficiently spectrally shifted towards the short wavelength region and bistable. These mutants will tolerate probing cell behavior using longer wavelength imaging and, thus, are suitable for controlling subcellular signaling.

Results and discussion

Broad spectral sensitivity of mMeOp

WT mMeOp has a λ^a_{max} between 440 and 480 nm [27, 65, 66] with an uncertainty due to purification and spectral characterization difficulties. In order to determine the λ^a_{max} value in-house, we expressed mMeOp with a carboxy-terminal 1D4 purification tag in HEK293S cells, purified the recombinant photopigment, and obtained the absorption spectrum as described previously [38, 67, 68]. Our experimental absorption maximum of showed a λ^a_{max} of ~470 nm (Fig. 1b). We then examined whether such λ^a_{max} makes mMeOp sensitive to different wavelengths by looking at the melanopsin-induced activation of both Gq and Gi/o pathways (Fig. 1c) [28]. Gq pathway activates Phospholipase Cβ (PLCβ), inducing the hydrolysis of plasma membrane-bound phospholipid, phosphatidylinositol 4,5-bisphosphate (PIP2) into inositol triphosphate (IP3) and diacylglycerol (DAG). To measure the ability of blue (445 nm), green (488 nm), yellow (515 nm), and red (594 nm) wavelengths to activate the melanopsin-Gq pathway, we employed PIP2 sensor (PH domain of PLCδ1) variants, each tagged with a different fluorescence protein, i.e., mTurquoise (mTq-434 nm), EGFP (484 nm), Venus (512 nm), or mCherry (587 nm), respectively (Fig. 1d). We expressed WT mMeOp and each PH sensor variant in HeLa cells. All experiments to examine the signaling of WT mMeOp and its mutants henceforth were conducted in the presence of 10 μM 11CR, and cells were imaged only using the wavelength of consideration, unless otherwise specified. Imaging of the PIP2 sensor using 445 nm (blue), 488 nm (green), 515 nm (yellow), and 594 nm (red) light resulted in similar and robust PIP2 sensor translocation from the plasma membrane to the cytosol, indicating PIP2 hydrolysis due to the Gq pathway and subsequent PLCβ activation (Fig. 1d images and plot). Moreover, to eliminate any contribution of Gi/o pathway activation, we performed the same experiment in the presence of Gi/o pathway inhibitor, 0.05 μg/mL pertussis toxin (Ptx). We observed robust and transient PIP2 hydrolysis with blue (445 nm), green (488 nm), yellow (515 nm), and red (594 nm) light colors even in the presence of Ptx (Figure S5). We used 1.5 μW laser powers to image each fluorescence protein. The observed PIP2 hydrolysis attenuation that occurred during 300 s is due to a mechanism we have recently explained[69]; however, it is not due to opsin deactivation. We showed that upon Gq-coupled GPCR activation, PLCβ is activated by the formation of GαqGTP–PLCβ–Gβγ complex, however, due to Gβγ dissociation, a significant attenuation of PIP2 hydrolysis occurs over time [69].

Next, we examined the Gi/o pathway activation by WT mMeOp in blue (445 nm), green (488 nm), yellow (515 nm), and red (594 nm) wavelengths using the Gγ9 translocation assay we developed to measure G protein activations at the subcellular, single-cell, and multi-cell levels (see Fig. 1e). This assay is based on the translocation of free Gβγ generated upon GPCR activation from

the plasma membrane to internal membranes, significantly increasing internal membrane fluorescence [70, 71].

Gγ9 has the most efficient translocation properties in the Gγ family [70, 71]. To eliminate any influence from the Gq pathway to Gγ9 translocation, we performed the experiments in the presence of the Gq inhibitor, YM-254890 (500 nM) [72]. Similar to the above Gq pathway assay, in the presence of 10 μM 11CR, we examined the translocation of mTq-Gγ9, GFP-Gγ9, Venus-Gγ9, or mCh-Gγ9 in HeLa cells also expressing mMeOp (Fig. 1e images and plot), indicating light-induced responses at all four wavelengths. As negative controls, we examined PIP2 hydrolysis and Gγ9 translocation in HeLa cells without melanopsin expression with blue, green, yellow, and red light in the presence of 10 μM 11CR. As expected, without melanopsin expression, we did not observe neither PIP2 hydrolysis (Figure S6) nor Gγ9 translocation (Figure S7) indicating melanopsin is responsible for the signaling responses observed in Fig. 1d, e.

We have previously demonstrated that the blue-centered absorption spectrum ($\lambda^{a}_{max} \approx 420$ nm) [73] of human cone blue opsin enables subcellular signaling activation using blue, and global response imaging using red wavelengths [6, 33]. However, the broad spectral sensitivity of mMeOp results in the activation of both Gq and Gi/o pathways even by 594 nm (red) light rendering it incompatible with subcellular signaling control. To capture melanopsin's Gq and Gi/o activity at 594 nm, we used mCh-PH and mCh-Gγ9, respectively. The observed sensitivity to long wavelengths may be ascribed to the high photoisomerization quantum yield (QY) of melanopsins [31] that causes the activation of biochemical processes even upon exposure to the tail region of the absorption spectrum where melanopsin has a low (but not negligible) absorbance. An investigation of the quantum yield of mMeOp at different spectral windows is beyond the scope of this work. Nonetheless, due to their similarity, a quantum yield of $\sim \gtrsim 50\%$ is hypothesized for mouse melanopsin as observed and computed for human melanopsin [31].

The WT mMeOp model

The protein-11CR interactions govern the absorption characteristics of opsins [74, 75]. This is because, as anticipated above, the λ^{a}_{max} value is inversely proportional to the vertical (i.e. measured or computed at a single equilibrium structure) energy difference between the first excited state S_1 and ground state S_0 (i.e., $\Delta E_{(S_1-S_0)}$) of 11CR. When considering the S_0 room-temperature equilibrium structure (i.e., the dark state), the opsin environment surrounding 11CR would produce a blue shifted λ''_{max} by stabilizing S_0 or/and destabilizing S_1 (see left part of the diagram in Fig. 2a). Of course, the opposite effects will generate a red-shifted λ'_{max} (see right part of the diagram in Fig. 2a).

The S_0 and S_1 stabilization or destabilization are primarily induced by the opsin electrostatics (i.e., the charge distribution created by the opsin residues surrounding 11CR) and conjugated backbone conformation (i.e., twisting of single and double bonds along the 11CR conjugated chain). The electrostatic modulation is possible because S_0 and S_1 have electronic structures with distinct backbone charge distributions (see Fig. 2b). More precisely, S_0 features a positive charge localized on the -C=NH- Schiff base linkage of 11CR, while S_1 features a positive charge delocalized away from the -C=NH- moiety (i.e., towards the chromophore β-ionone ring). The conformational modulation is instead explained by the modification of the electronic structure imposed by the twisting about single bonds decreasing the conjugation (i.e., leading to a blue-shift) or by the twisting about

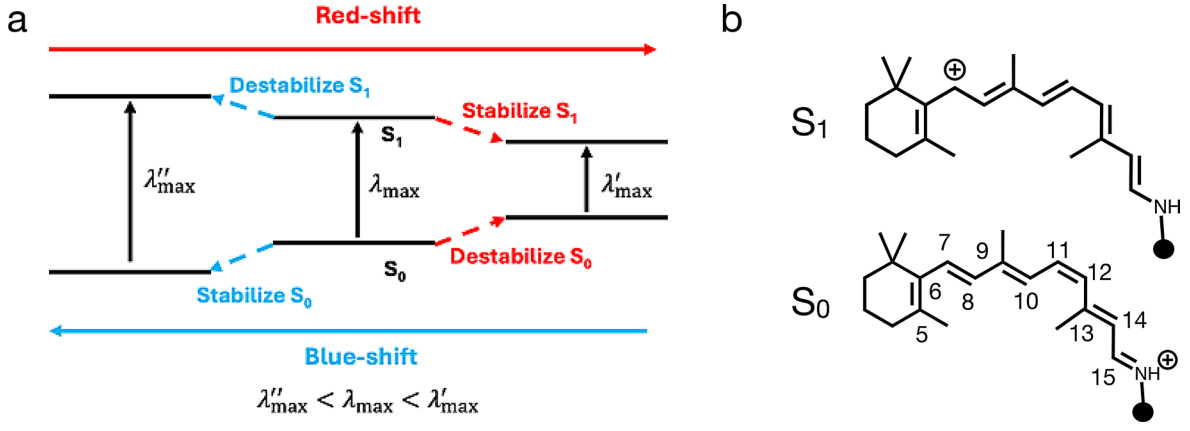

Fig. 2 Tuning of the retinal chromophore absorption maximum. **(a)** Scheme for the blue-shifting (towards the shorter wavelength side) and red-shifting (towards the longer wavelength side) effects. **(b)** Electronic structure and charge distribution of the retinal chromophore on the ground (S_0) and first excited state (S_1). The terminal circle in each structure represents the covalent linkage to the protein. The conventional numbering of the chromophore atoms is also given

double-bonds causing a weakening of the π-bond (i.e., leading to a red-shift) [53].

A realistic (i.e., accurate enough) QM/MM model of WT mMeOp is crucial when searching for in silico mutations capable of spectrally shifting it towards the blue region and, hopefully, resisting activation by red light. A realistic model could lead to the understanding of the protein-11CR interaction allowing for an educated guess of mutations that induce a spectral shift toward the shorter wavelength region. On the other hand, the construction of models of the guessed mutants can increase confidence in the prediction and provide information on the extent of the blue-shifting effect. The construction of a QM/MM model always starts from some static structure. In the case of the absence of WT structural data (i.e., of an x-ray crystallographic or Cryo-EM structure), we exploited the ∼40% sequence similarity between squid rhodopsin (SqRh, with an x-ray crystallographic structure available as PDB ID 2Z73) and mMeOp to produce a homology model using the MODELLER program [76]. Among an ensemble of ∼thousand models generated with MODELLER, the homology model with the highest 3D profile and quality scores was selected, refined by adjusting side-chain torsion angles, and optimized by CHARMM force field [77], utilizing the implicit generalized Born membrane/water model [76, 78]. The retinal-lysine fragment, the counterion, and water molecules of both the selected homology model of WT mMeOp and the crystallographic structure of WT SqRh are shown in Fig. 3a. To computationally investigate the spectral features of mMeOp, we used the homology model above as the input to the ARM protocol [78] to generate ten QM/MM models. Such models are then used to predict the λ^{a}_{max} value of mMeOp in terms of their average vertical excitation energy $\Delta E_{(S_1-S_0)}$ that is converted in λ^{a}_{max} via the well-known relationship, $\lambda^{a}_{max}=hc/\Delta E_{(S_1-S_0)}$ where h is the Planck's constant and c is the speed of light. The most important residues in the cavities of the QM/MM models of WT SqRh and WT mMeOp are given in Fig. 3b, where similar protein-retinal interactions for the two opsins are shown. In SqRh, the H-bond network between E180, Y277, and S187 residues holds the counterion E180 close to the Schiff base nitrogen (SBN) and, thus, stabilizes S_0. Also, N87 and Y111 stabilize the S_0 as their dipoles are oriented toward the SBN (Fig. 3b). The cavity of mMeOp exhibits a H-bond network between S221, Y309, and E214, conserved from SqRh, and it extends to Wat-1, which does not affect

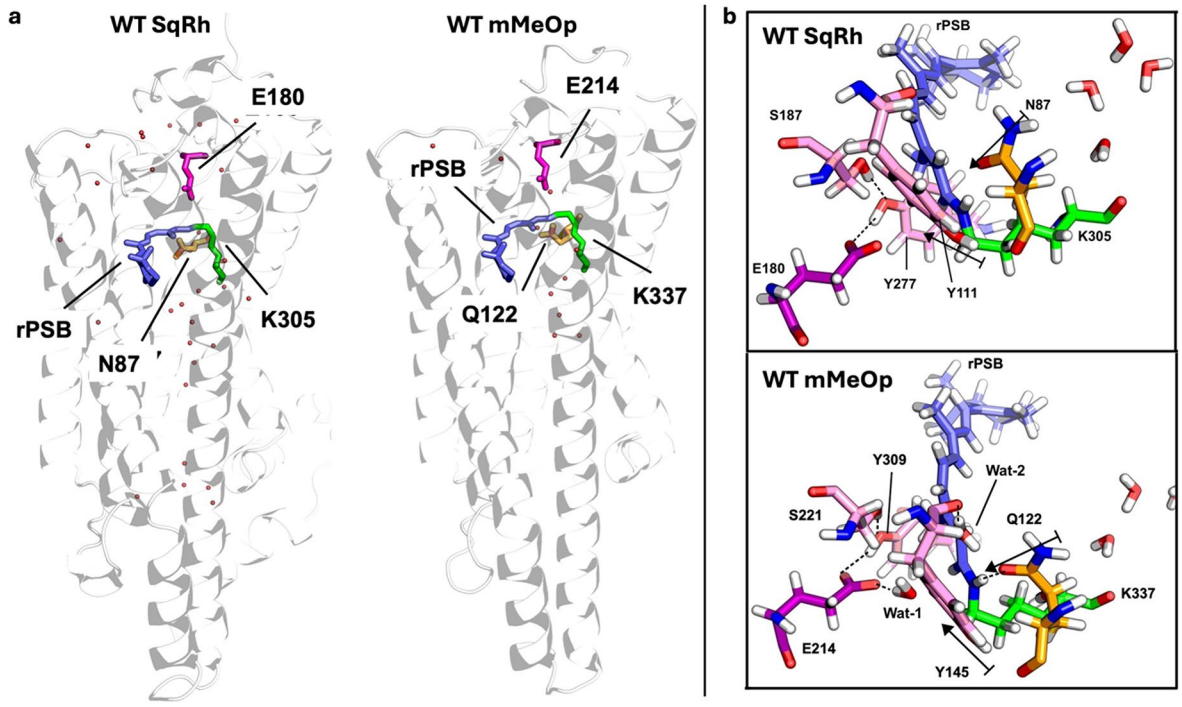

Fig. 3 WT SqRh and mMeOp. **(a)** Comparison of the retinal-lysine fragment, counterion, and water molecules from the crystallographic structure of squid rhodopsin (SqRh, PDB ID 2Z73) and the selected homology model of mouse melanopsin (mMeOp). Retinal protonated Schiff base (rPSB) chromophores are shown in blue color, retinal binding sites (K305 in SqRh and K337 in mMeOp) are shown in green, main counterions (E180 in SqRh and E214 in mMeOp) are shown in purple, secondary counterions (N87 in SqRh and Q122 in mMeOp) are shown in orange, and red dots indicate water molecules. **(b)** Comparison of the retinal binding cavities of QM/MM ARM models for WT SqRh and WT mMeOp. The retinal and the Schiff-base forming lysine are shown in blue and green, respectively. The primary and secondary counterions are shown in purple and orange, respectively. Other residues stabilizing the S_0 are shown in pink. Labels Wat-1 and Wat-2 correspond with the number of water molecules in the active site of WT mMeOp. The dashed lines and black arrows correspond to H-bonds and dipole moment orientations, respectively

the conformational relaxation of the counterion. As a consequence, the negatively charged E214 may cooperate with the dipole moment of Wat-1 to provide further electrostatic stabilization of S_0 in mMeOp by stabilizing the positive charge on the C15=N moiety of 11CR (see Fig. 2a). Similarly, one may expect that Wat-2 stabilizes S_0 that is, H-bonded to the carbonyl of the backbone of Y145 (Fig. 3b).

In order to assess the accuracy of our protocol for SqRh and mMeOp, we compared the computed $\Delta E_{(S_1-S_0)}$ to the experimental quantities. The calculated results display the correct trend (see full line in Fig. 4) with the same slope with respect to the experimental data due, mainly, to a ca. 2 kcal/mol overestimated excitation energy. This type of difference is consistent with the general error bar of ARM models [53, 78].

Since the computed excitation energies of both WT mMeOp and SqRh reproduce the experimental values with a relatively small error, we use the corresponding QM/MM models to investigate λ^{a}_{max} in terms of (i) electrostatic interactions between the cavity and the 11CR and (ii) the steric effect of the cavity on 11CR. In order to disentangle these effects [79, 80], we compared the $\Delta E_{(S_1-S_0)}$values of 11CR (taken with its cavity-optimized conformation), calculated in the protein environment ($\Delta E_{(S_1-S_0)}$ Protein Environment) and in vacuo ($\Delta E_{(S_1-S_0)}$ Vacuo). Such comparison (summarized in Table S2) shows that in-vacuo excitation energies for SqRh and mMeOp are ~11 and ~15 kcal/mol lower than inside the opsin, respectively. This indicates strong electrostatics in both opsin cavities triggering spectral shifts towards the short wavelength region. Table S2 also suggests that the electrostatic effect is mainly responsible for the 2.9 kcal/mol blue-shifting exhibited by mMeOp with respect to SqRh. In fact, it is evident from the table that the conformational contribution alone ($\Delta E_{(S_1-S_0)}$ Vacuo) would rather lead to mMeOp having a red-shifted λ^{a}_{max} compared to SqRh, contrary to the computed ΔE_{S1-S0} value for the complete protein model.

Animal opsins usually undergo ultrafast (i.e., subpicosecond) isomerization characterized by ultrashort S_1 lifetimes. This has been measured for Bovine and Octopus rhodopsins with an S_1 lifetime of less than 100 fs [81]. It has also been computationally found that both SqRh and human melanopsin (hMeOp) undergo S_1 to S_0 decay within 100 fs [31]. More in general, blue-shifted rhodopsins are thought to be associated with shorter S_1 lifetimes due to the increased kinetic energy gained during S_1 torsional relaxation toward the S_1/S_0 conical intersection (CoIn) funnel [54, 82] delivering the chromophore to S_0 (see Fig. 5). On the contrary, proteins with absorption shifted towards longer wavelength values are expected to exhibit a longer S_1 lifetime [54]. Before employing the WT mMeOp model in mutational studies, it is important to further validate it by looking at the predicted lifetime. To do so, we performed deterministic quantum-classical Franck-Condon (FC) trajectories, namely surface-hop trajectories released on the S_1 potential energy surface starting from the S_0 equilibrium structure with zero initial velocities and decaying to S_0 when the decay probability is >0.5 (i.e.without using a random number generator). Since we are only interested in the opsin evolution on S_1, the trajectories were propagated until entering the region of an S_1/S_0 CoIn, where

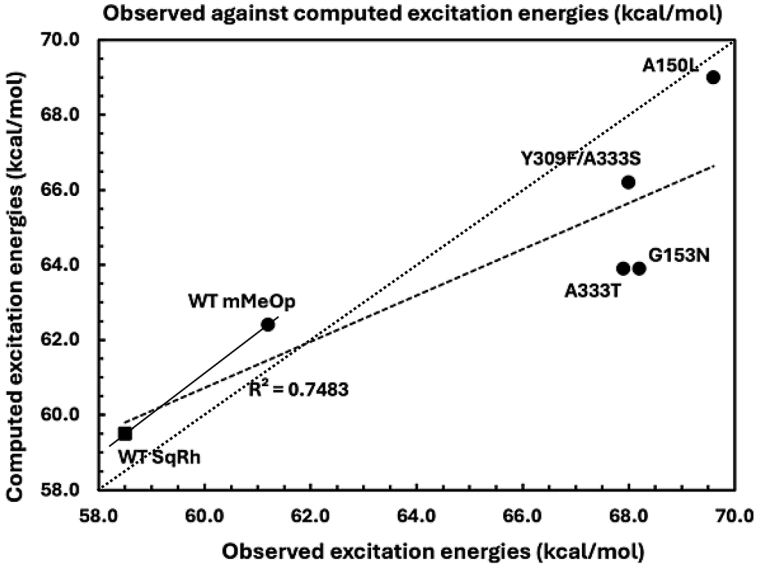

Fig. 4 Accuracy of the QM/MM models. Correlation plot for the excitation energies (kcal/mol) of WT SqRh, WT mMeOp, and mMeOp mutants. The full line is used as an eye guidance to assess the difference between computed and experimental (dotted line) trends for the WT forms. The fitting (dashed) line and the correlation factor R^2 are shown

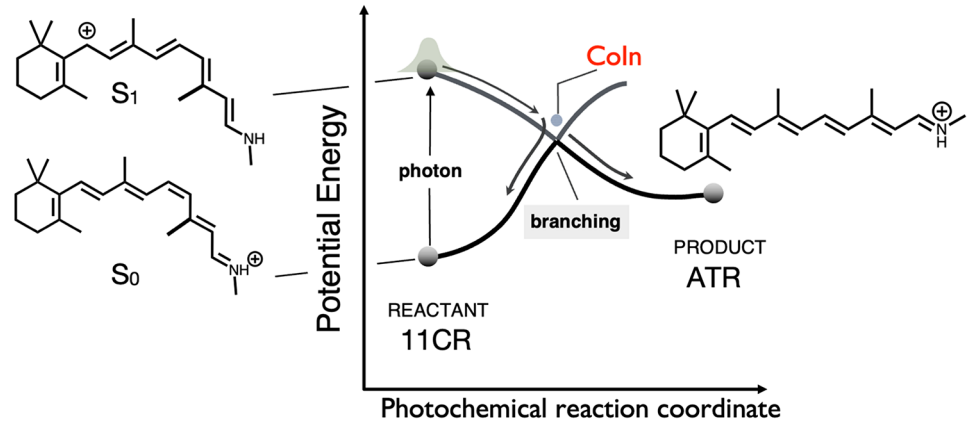

Fig. 5 Schematic representation of the ultrafast 11-*cis* to all-*trans* isomerization (from 11CR to ATR pointing to the isomerization of the C11 = C12 bond) of the retinal chromophore occurring via the conical intersection (CoIn) between S_1 and S_0. At decay, a branching occurs that results in only a fraction of the population relaxing towards the ATR product

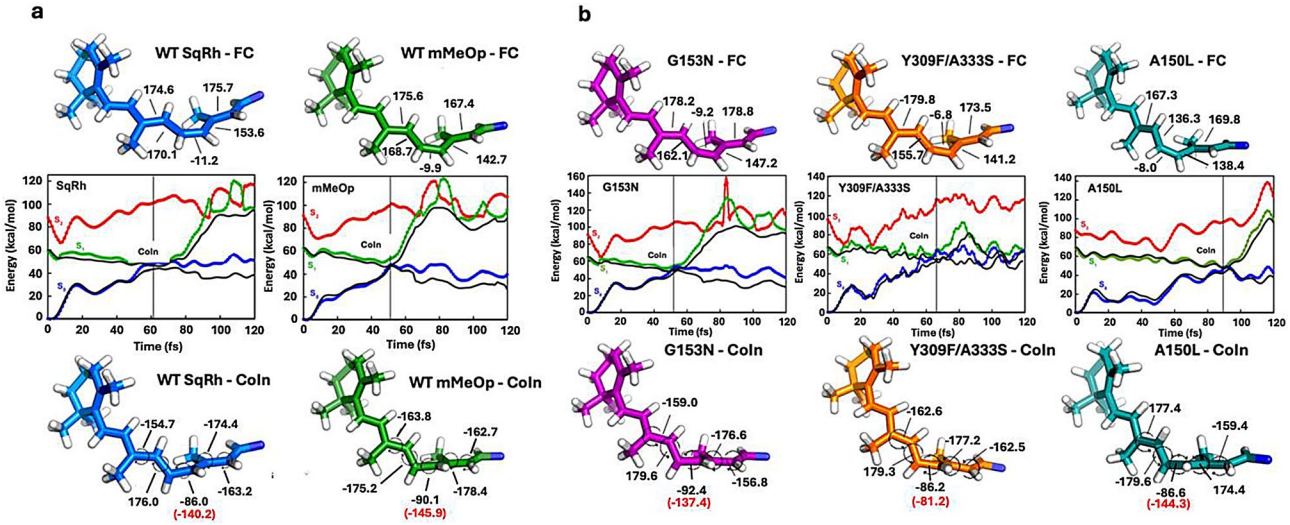

Fig. 6 Dynamics of the 11CR chromophore photoisomerization **(a)** QM/MM trajectories of SqRh and melanopsin-WT ARM models, computed at the two root SA-scaled CASSCF(12,12)/6-31G*/Amber (black lines) level of theory and corrected at 3 root CASPT2 level. S_0 (blue lines), S_1 (green lines), and S_2 (red lines). Franck-Condon geometries are at the top, and conical intersection (CoIn) geometries are at the bottom for each studied opsin. Dihedral angles are given in degrees. The dihedral angle of the C11-C12 bond at 120 fs is given in red, indicating that the isomerization is leading toward the photo-product (all-*trans* retinal) with a dihedral angle of the C11-C12 bond equal to ~180 degrees. **(b)** QM/MM trajectories of G153N and A150L melanopsin mutants' ARM models, computed at the two root SA-scaled CASSCF(12,12)/6-31G*/Amber (black lines) level of theory and corrected at 3 root CASPT2 level. S_0 (blue lines), S_1 (green lines), and S_2 (red lines). Franck-Condon geometries are given at the top, and conical intersection geometries are provided at the bottom for each studied opsin. Dihedral angles are given in degrees. The dihedral angle of the C11-C12 bond at 120 fs is given in red, indicating that the isomerization is leading toward the photo-product (all-*trans* retinal) with a dihedral angle of the C11-C12 bond equal to ~180 degrees. Notice that the single dynamic computed to investigate the photoisomerization of Y309F/A333S retinal leads back to the 11-*cis* reactant. Nonetheless, this behavior is not unexpected as the quantum yield of this process is not equal to one

decay to S_0 occurs, and formation of the ATR chromophore (i.e., the isomerization product) is initiated. The FC trajectories of SqRh and mMeOp WT models are shown in Fig. 6a. Both models decay within ~70 fs; however, melanopsin reaches the hop point ~10 fs earlier than SqRh: a result consistent with previous computational studies on human melanopsin [31]. A blue-shifted λ^{a}_{max} suggests a larger S_1 destabilization and, therefore, a shorter S_1 lifetime (i.e., as reported in Table S1). Consistently, the $\Delta E_{(S_1-S_0)}$ value of the mMeOp model is larger than that of the SqRh model and thus, a higher speed of the mMeOp S_1 relaxation and photoisomerization is expected [54, 83]. As apparent from the comparison of the 11CR representations in Fig. 6a, the mMeOp retinal geometry shows the lowest root mean squared deviation (RMSD) value (0.13966) between its FC and CoIn geometries and an average S_1-S_2 gap (energy difference between the first (S_1) and second (S_2) excited state) value similar to SqRh (the S_1-S_2 gap may contribute to slowing the dynamics down) [84]. Therefore, even from the

geometrical viewpoint, mMeOp would need less time to reach the CoIn than SqRh. Below, we show how we have conveniently used the validated mMeOp model to predict a small set of blue-shifting mutations expected to simultaneously decrease the sensitivity to red light and the isomerization timescale.

Modeling, cavity analysis, and trajectory analysis of potentially blue-shifted melanopsin mutants

Decreasing the sensitivity of the opsin to red light requires mutations that alter the interaction of the 11CR with the surrounding environment [53, 54, 78, 85] in such a way to shift the λ^{a}_{max} value to the blue. By using the WT mMeOp homology model as a template and the ARM protocol, we have obtained the QM/MM models of eight single-point and two double-point blue-shifted mutants from a pool of mutations that could potentially either stabilize S_0 or destabilize S_1 (see Fig. 2 and related discussion above) via electrostatic and steric effects (see the Supplementary Information for details). The QM/MM models of the ten selected mutants predicted a 5–42 nm blue shift in λ^{a}_{max} with respect to the WT model. The model accuracy is assessed by comparing the computed and observed λ^{a}_{max} values (see Fig. 4 with a correlation factor R^2 of ~0.8 when also including in the set of the WT SqRh and WT mMeOp). Figure 7a shows the potential mutation sites and water molecules, and Fig. 7b shows the short wavelength-shift in $\Delta E_{(S_1-S_0)}$ for each mutant model. A150L and Y309F produced the largest shifts. Considering the blue-shifting effect of G153N and A333T, we constructed QM/MM models for A333S, A333N, and G153V. However, the effect of such mutations was less than expected. Larger blue-shifting effects were expected for double-point mutations, hypothesizing additivity. However, only Y309F/A333S shows such an effect with respect to Y309F, while the A150L/Y309F has a smaller short wavelength shift than A150L alone.

In order to estimate the magnitude of the electrostatic and steric effects associated with each mutation, we recomputed their $\Delta E_{(S1-S0)}$ after zeroing the charges of the mutated residues (Figure S1) and *in-vacuo* (see Figure S2 and Table S4). These calculations allowed identifying the mutations dominated by short wavelength -shifting steric interactions (Fig. 8) and those dominated by blue-shifting electrostatic effects (Fig. 9). Such analysis shows that A150L mutation results in cavity-induced 11CR geometrical changes generating a small long wavelength shift (~0.5 kcal/mol) in $\Delta E_{(S_1-S_0)}$. While electrostatic interactions increase $\Delta E_{(S_1-S_0)}$ by ~7 kcal/mol (see Figure S2 and Table S4). That is, the electrostatic effects are responsible for the overall ~6.5 kcal/mol short wavelength-shift with respect to the WT mMeOp model. For Y309F, the electrostatic interaction dominates the computed blue shift (Table S4). In the A150L/Y309F mutant, the inserted bulkier side chains twist the 11CR conjugated chain into a long wavelength shifted (~1 kcal/mol) configuration resulting from double bond distortion. At the same time, the electrostatic cavity-11CR interaction produces a dominating (~6.7 kcal/mol) blue shift. Furthermore, It was found that Y309F, Q122N, A333T, A333S, and Y309F/A333S mutants only slightly affected the retinal chromophore conformation (Figure S2 and Table S4) and that it is the change in side-chain polarity that increases the S_1-S_0 energy gap (Figure S1 and Table S4).

In contrast, the A333N, G153N, and G153V mutants display a blue-shifting effect caused by sterically induced changes in the 11CR conformation (see Figure S2 and Table S4). For instance, the N153 residue largely twists

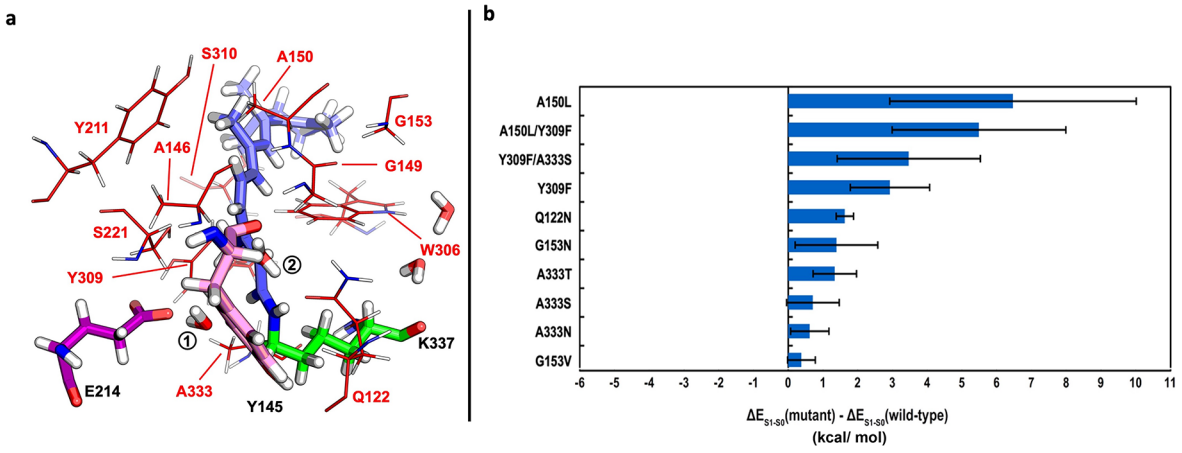

Fig. 7 Cavity residues and short wavelength shifting effect of the mMeOp ARM model. **(a)** Cavity residues of ARM model of melanopsin. Selected amino acids for point mutations are shown in red. The retinal chromophore is shown in blue, the lysine linker (K337) in green, and the primary main counterion (E214) in purple. Water molecules are labeled as Wat-1 and Wat-2. **(b)** Effect of mutations on the λ^{a}_{max} of mMeOp, computed as the difference in $\Delta E_{(S_1-S_0)}$ between mutant and WT models. Blue bars correspond to the short wavelength-shift in the absorption maximum. Black lines are standard deviations

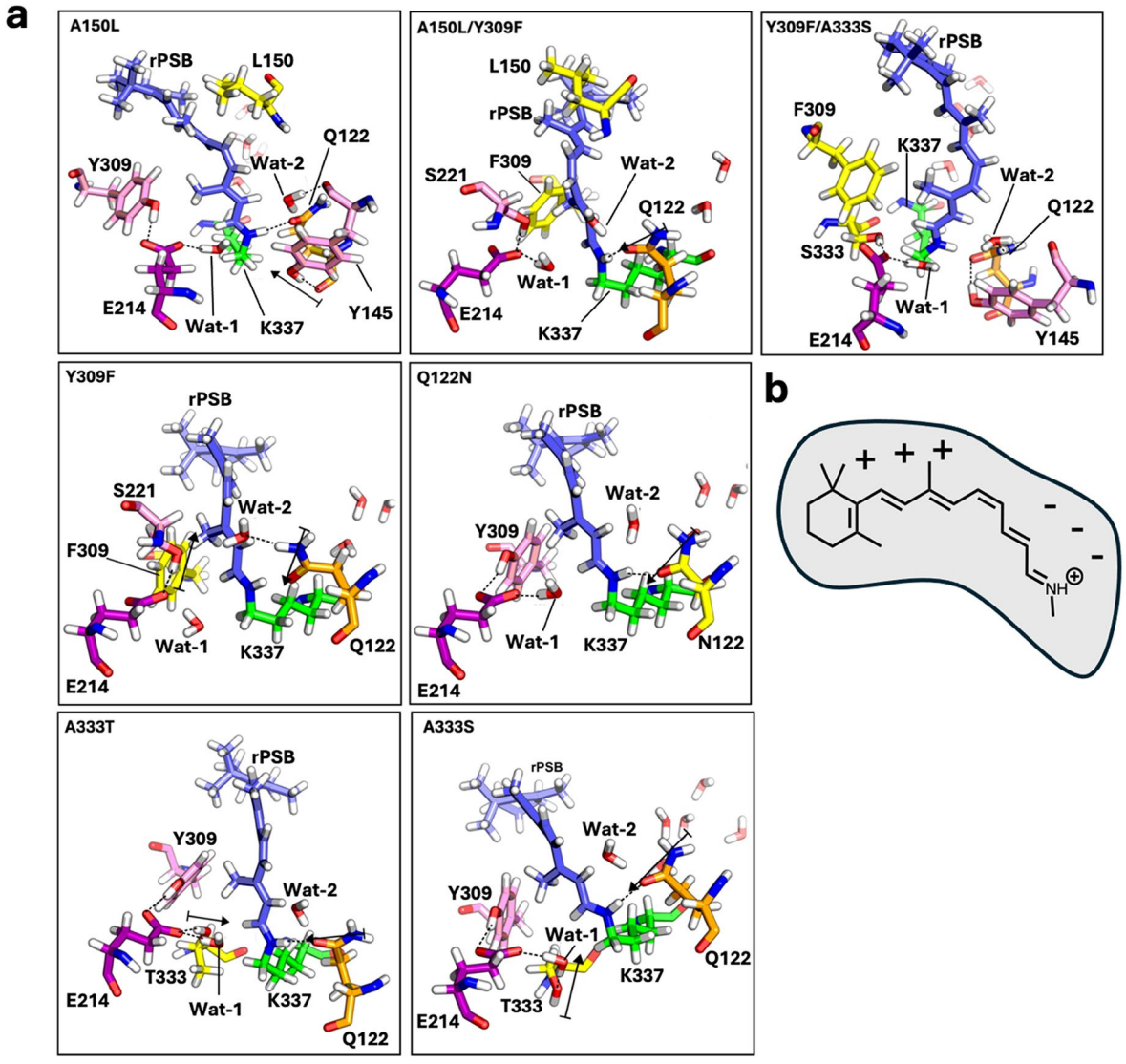

Fig. 8 Cavities of the blue-shifted mutants due to electrostatic effects. **(a)** The mutated residues (yellow) modulate $\Delta E_{(S_1-S_0)}$ mainly via electrostatic interactions. The black dotted lines and black arrows indicate H-bonds and dipoles, respectively. **(b)** Schematic representation of blue-shifting electrostatic effects via S_0 stabilization and S_1 destabilization (see also Fig. 2)

the single bonds of 11CR (Figure S3) and hence, the computed λ^{a}_{max} value decreases with respect to the WT (Figure S2).

To qualitatively estimate the S_1 lifetime of the mutants and provide evidence supporting a functional opsin (i.e., with an S_1 lifetime similar to the one of the WT model), we computed the corresponding FC quantum-classical trajectories. In the past, short S_1 lifetimes were assumed to indicate high sensitivity (i.e., high isomerization QY) consistently, with the Landau-Zener model relating faster isomerization with higher sensitivity [86]. However, it has been recently demonstrated, by computing entire sets of quantum-classical trajectories representing the opsin's S_1 population dynamics, that while vertical excitation energies and excited state lifetimes are inversely proportional, excited state lifetimes and isomerization QY are not proportional [31]. The reason for this behavior was demonstrated to be related to the fact that the Landau-Zener model strictly applies to the reaction coordinates in the decay region [87], which could be different from the usually assumed reaction coordinate described exclusively by double-bond twisting.

FC trajectory calculations were performed for three diverse blue-shifted mutants: G153N, A150L, and Y309F/A333S. None of the mutants displayed a decreased S_1 lifetime that remained of the same magnitude as the WT. The G153N mutant reaches the CoIn at ~53 fs, while the A150L and Y309F/A333S mutants enter the CoIn region after ~90 fs and ~66 fs, respectively (see Fig. 6b). As stressed above, these results are only qualitative and

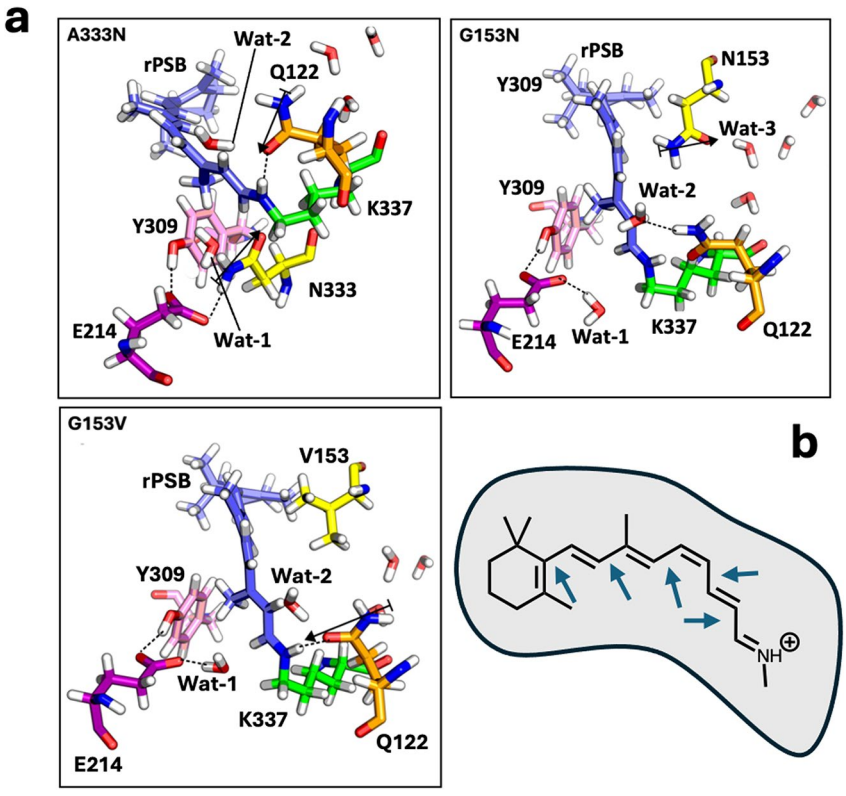

Fig. 9 Cavities of the blue-shifted mutants due to steric effects. **(a)** The mutated residues (yellow) modulate $\Delta E_{(S_1-S_0)}$ mainly via steric interactions. The black dotted lines and black arrows indicate H-bonds and dipoles, respectively. **(b)** Schematic representation of steric (geometrical) blue-shifting effect associated to torsion about single bonds

cannot be used to predict "observed" lifetimes. Such a prediction would only be possible after running a statistically significant number of trajectories (hundreds) starting from different initial conditions [54]. Such demanding calculations go beyond the scope of the present research.

In the case of A150L, the trajectories (Fig. 6b) indicate that the longer S_1 lifetime is not consistent with the top short wavelength-shifted $\Delta E_{(S_1-S_0),}$ but it is consistent with the larger difference between the FC and CoIn geometries. However, geometrical considerations alone cannot explain why G153N and Y309F/A333S display a slower speed with respect to the WT. However, in these two cases, the computation of CASPT2 energies revealed a ~4 kcal/mol S_1-S_2 gap, which strongly increases the possibility of interaction between these two states that has been associated with a slower isomerization [84]. Again, it must also be pointed out that the above considerations are qualitative since they are based on a single FC trajectory.

Spectral sensitivity and signaling of the predicted blue-shifted melanopsin mutants

Using site-directed mutagenesis, we generated the ten in silico-predicted short wavelength-shifted melanopsin mutants of Fig. 7b. Next, we used live cell imaging, and examined whether the mutants (i) were sufficiently short wavelength-shifted to resist activation by red light (594 nm) and (ii) possessed signaling activities similar to the WT exposed to wavelengths < 500 nm. The 594 nm (1.5 µW) choice is imposed by the fact that such wavelength is used in cell imaging and, as also mentioned above, one wants to avoid melanopsin activation in that irradiation condition. We first tested Gq signaling by expressing each melanopsin mutant using mCh-PH in HeLa cells, and mutants that did not show PIP2 hydrolysis upon red light irradiation were selected for subsequent screening. We found that only the six mutants A150L, G153N, G153V, A333T, Y309F/A150L, and Y309F/A333S did not respond to red light activation (see Fig. 10a and Figure S4) not showing PIP2 hydrolysis.

We next examined whether the six red-light-resisting mutants could sense blue light and activate signaling. Similar to what was reported in Fig. 1d, we expressed each of the six melanopsin mutants alongside mTq-PH in HeLa cells. G153V and Y309F/A150L expressing cells did not show PIP2 hydrolysis when exposed to 445 nm, 1.5 µW, light (see Figure S4 e and f), indicating a complete loss of activity. On the other hand, the cells expressing the four mutants A333T, A150L, G153N, and Y309F/A333S showed robust PIP2 hydrolysis upon 445 nm,

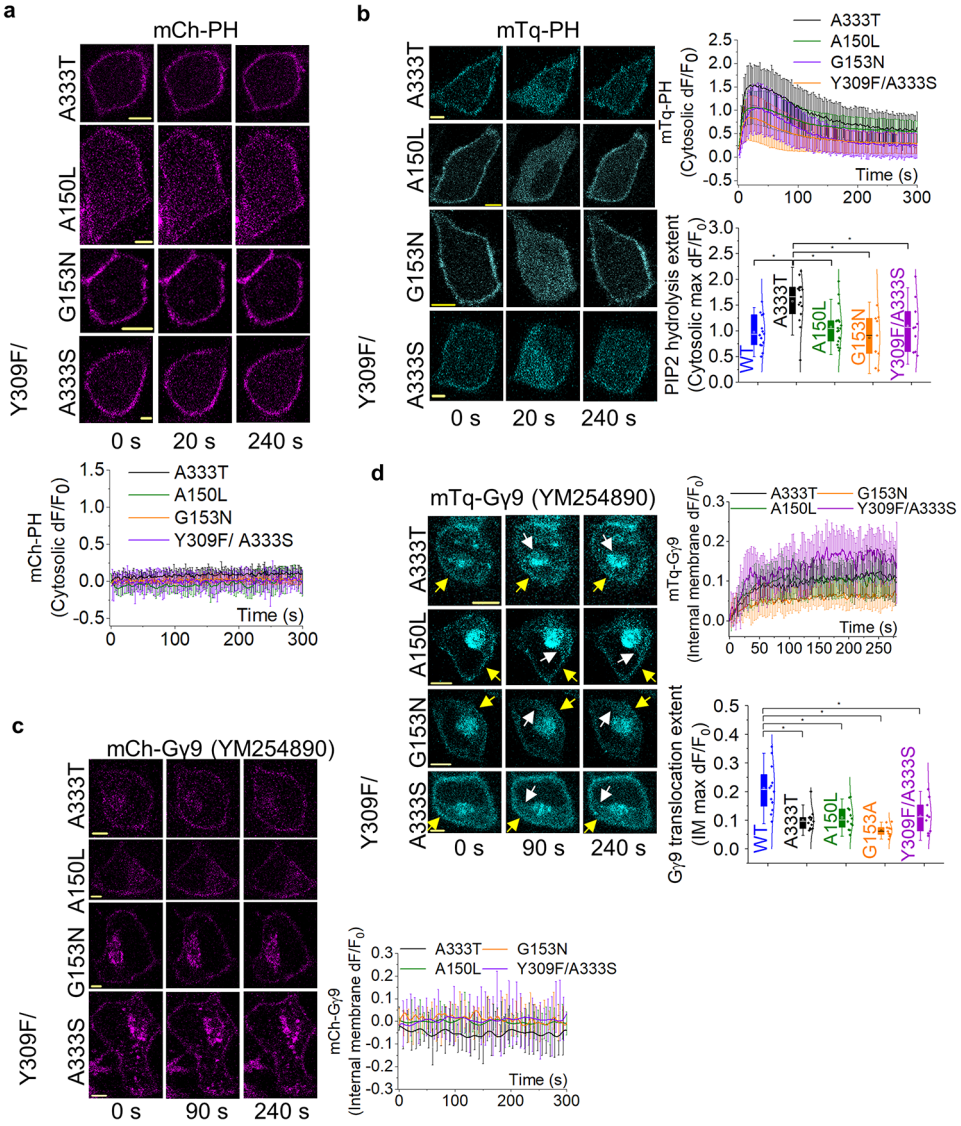

Fig. 10 Melanopsin blue-shift mutants exhibit robust Gq and Gi/o activity in blue light but resist red light-induced activation. **(a)** Red light did not induce detectable hydrolysis of PIP2 with any of the mutants. A333T (n = 11), A150L (n =11), G153N (n = 8), and Y309F/A333S (n = 11). **(b)** HeLa cells expressing mTq-PH alongside melanopsin-blue-shift mutants; A333T (n = 15), A150L (n = 19), G153N (n = 9), Y309F/A333S (n = 10) exhibit robust PIP2 hydrolysis upon photoactivation by blue light in the presence of 10 µM 11CR. Images and the corresponding plot show the PIP2 sensor dynamics in the cytosol. The whisker box plot shows the PIP2 hydrolysis extent of each mutant and WT. **(c)** A333T, A150L, G153N, and Y309F/A333S mutants resist photoactivation by red light (n = 12: A333T, 9: A150L, 10: G153N, 11: Y309F/A333S). **(d)** HeLa cells expressing mTq-Gγ9 alongside melanopsin-blue-shift mutants; A333T, A150L, and G153N, and Y309F/A333S exhibit Gγ9 translocation from the PM to IMs upon photoactivation by blue light in the presence of 10 µM 11-*cis*-retinal and the Gq inhibitor, YM254890. White and yellow arrows indicate the fluorescence intensity increase on IMs and the loss of fluorescence intensity on the PM, respectively. The corresponding plots show Gγ9 dynamics on the IMs (n = 13: A333T, 12: A150L, 11: G153N, 9: Y309F/A333S). The whisker box plot shows the Gγ9 translocation extent of each mutant and WT. Average curves were plotted using 'n' cells, n = number of cells. Error bars represent SD (standard deviation). Statistical comparisons were performed using One-way-ANOVA; p<0.05, (*: population means are significantly different). The scale bar = 5 µm.; mTq: mTurquoise; mCh: mCherry; max: maximum

blue light irradiation (Fig. 10b). Comparing the extent of PIP2 hydrolysis induced by WT mMeOp with each active mutant, we notice that A333T induced a significantly higher signal, while A150L, G153N, and Y309F/A333S mutants showed PIP2 hydrolysis close to the WT (Fig. 10b, whisker plot, One-way ANOVA: $F_{4,62}$ = 5.35772, p=9.67E-4, Table S5 a and b).

Since WT mMeOp activates both Gq and Gi/o pathways efficiently [88], we tested whether the four mutants also induce efficient Gi/o signaling upon blue light in the presence of Gq inhibitor, YM-254890. All four mutants showed Gγ9 translocation upon blue light exposure (Fig. 10d). However, compared to the WT, the Gγ9 translocation responses of the mutants were significantly

lower (Fig. 10d, whisker plot, One-way ANOVA: $F_{4,55}$ = 22.38526, p=1.02508E-10, Table S6 a and b), indicating a reduced Gi/o activity. In a control experiment, we observed that these mutants did not show Gγ9 translocation when exposed to red light (Fig. 10c). Notice that the G153N mutant exhibited the lowest Gq and Gi/o activity of all, indicating the mutation in the retinal binding cavity has compromised its overall activity (Fig. 10b and d, whisker plots).

Spectral characterization of red light-resisting melanopsin mutants

To determine the absorption spectra of the four red-light-resisting mutants selected above (A333T, A150L, G153N, and Y309F/A333S), we expressed and purified them in HEK293S cells. The absorption spectrum for A333T yielded a λ^a_{max} of ~450 nm (~20 nm blue-shifted with respect to the WT mMeOp (see Fig. 11a) and substantially unmodified under light-adapted and dark-adapted conditions (see Fig. 11b). However, it was not possible to determine the spectral blue shift of other mutants using absorption spectroscopy, likely due to low stability in detergent. Therefore, we determined their action spectra by measuring Gq pathway activation-induced Ca^{2+} mobilization upon activation at wavelengths ranging from UV to red using the aequorin reporter assay [89, 90]. In the presence of 5 μM Coelentrazine-H substrate and 10 μM 11CR, the baseline luminescence readings were collected from HeLa cells expressing mMeOps (WT, A333T, A150L, G153N, or Y309F/A333S) and aequorin. Afterward, each well was exposed to near monochromatic light of the selected wavelength while collecting aequorin luminescence. We captured luminescence data at ~20 different wavelengths spanning the 230–700 nm range.

We observed wavelength-dependent aequorin luminescence increase for the WT form and all mutants. These were fitted with the predicted absorbance spectrum for opsin: vitamin A-based photopigments from the Govardovskii template [91]. The action spectra of the WT mMeOps showed a maximum (i.e., the estimated λ^a_{max}) of 486 nm (Fig. 11c), a value relatively close to the 470 nm λ^a_{max} obtained from its absorption spectrum, justifying the use of action spectra derived λ^a_{max} in these opsins [89]. Consistent with such a conclusion, the A333T mutant showed an estimated λ^a_{max} at 421 nm (Fig. 11b) and, therefore, a 65 nm shift towards the short wavelength region compared to the WT. This difference is significantly larger in magnitude than the differences in measured λ^a_{max}, but confirms the short wavelength shifting effect of the mutation. (Notice that the differences between absorption spectra and the corresponding action spectra can be partially due to the protein environment differences between detergent and living cells). Action spectra of the A150L, G153N, and Y309F/A333S mutants showed λ^a_{max} of 411 nm (75 nm blue-shift), 426 nm (60 nm blue-shift), and 420 nm (66 nm blue-shift), respectively (see Table S3 and Fig. 11c). Although it was not possible to directly measure the spectral shift for these three mutants, the observed shifts appear to be similar to the one measured for A333T, suggesting that these mutants may not respond to red light due to their blue-shifted absorption and reduction in long-wavelength pigment sensitivity.

Blue-shift melanopsin mutants are bistable

Since the engineering of subcellular signaling-capable optogenetic opsins is a key goal of this work, we examined whether A333T, A150L, G153N, and Y309F/A333S possess bistability. When irradiated, bistable opsins in their dark-adapted state (i.e., kept in the dark until fully equilibrated), a stable photoproduct is generated, resulting in a usually slightly altered absorption spectra [92]. It has been shown that WT mMeOp forms a stable photoproduct with a red-shifted absorption spectrum [30]. While we could not obtain resolved dark or light-irradiated spectra for A150L, G153N, and Y309F/A333S (see above), the light-irradiated spectrum of the A333T mutant indeed showed a spectrum similar to that of the dark-adapted state (Fig. 11b, red plot). This indicated that the A333T mutant is bistable suggesting that, to some extent, the other mutants are likely to be bistable.

The functionality of the four mutants was also tested by looking at the ability to allow prolonged signaling under limited chromophore concentrations; a characteristic feature of most bistable opsins. We hypothesized that at a low enough 11CR concentration, a monostable opsin should show only a transient signaling activity, while the bistable opsins will show sustained signaling. Since PIP2 hydrolysis shows inherent signaling attenuation, as explained earlier, we used the Gγ9 translocation assay to examine sustained signaling in bistable opsins. We used well-characterized monostable human cone blue opsin (BO) and bistable lamprey parapinopsin (LPO) expressing cells to validate the assay. In the presence of a relatively low concentration of 11CR (50 nM), BO-expressing cells showed a robust, however, transient mTq-Gγ9 translocation from the plasma membrane to endomembranes upon exposure to blue light (Fig. 11d: BO and plot). On the contrary, under the same 11CR availability, bistable LPO showed a sustained Gγ9 translocation (Fig. 11d: LPO and plot). We calculated the attenuation/recovery percentage of the Gγ9 translocation for both BO and LPO in the presence of blue light with 50 nM 11CR. Although the Gγ9 translocation attenuation was negligible with LPO, BO-induced Gγ9 translocation showed a significantly higher attenuation of 67.8±3.0% (Fig. 11d, whisker plot, One-way ANOVA: $F_{1,23}$ = 384.92321, p=7.35E-16, Table S7 a and b). As a control, when we

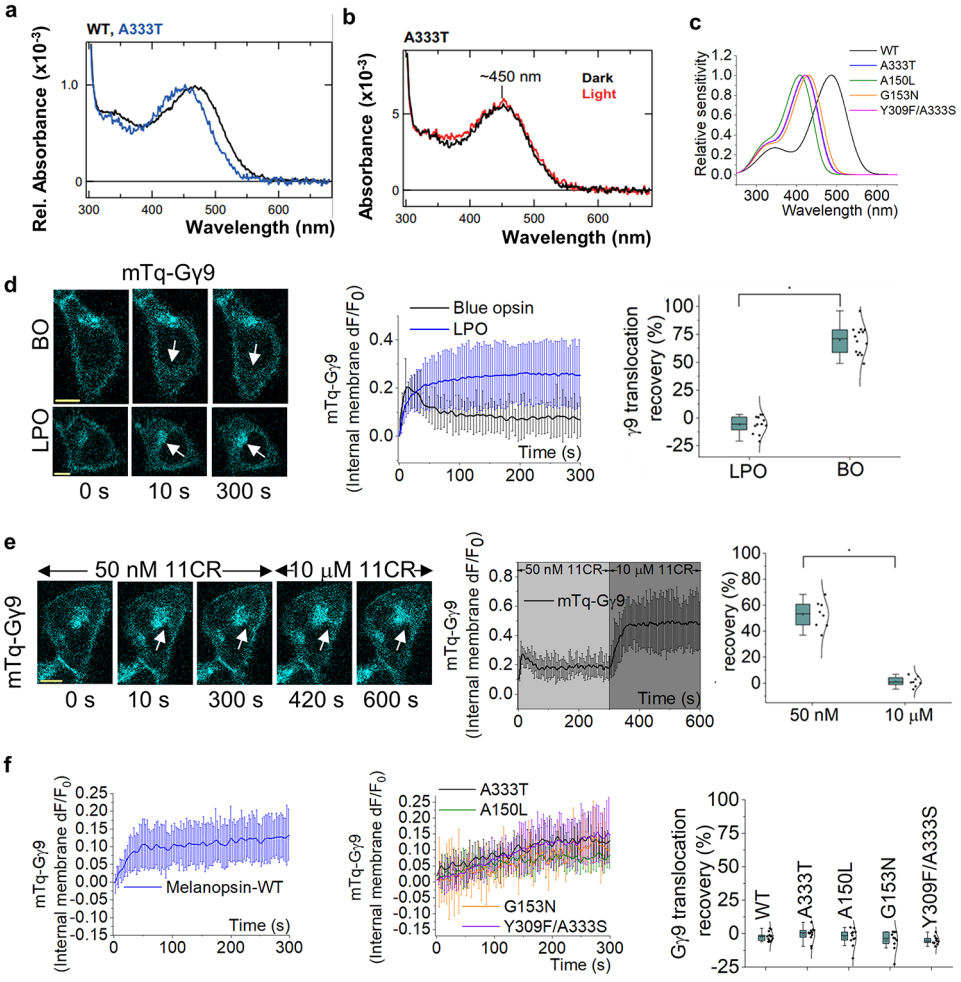

Fig. 11 Experimental absorption and action spectra of melanopsin mutants show significant blue shifts compared to the WT and are bistable. **(a)** Comparison of the WT and A333T mutant melanopsins' absorption spectra show a ~20 nm blue shift in A333T. The blue and black plots indicate the absorption spectra of melanopsin-A333T and WT-melanopsin, respectively. (**b)** Purified melanopsin-A333T mutant from heterogeneously expressed HEK293S cells exhibited a λ^{a}_{max} of ~450 nm in the dark (black plot). The light-exposed spectrum of melanopsin-A333T was nearly identical to the dark spectrum with a similar λ^{a}_{max} (red plot). **(c)** The fitted action spectra of A333T, A150L, G153N, and Y309F/A333S-melanopsin exhibit significant blue shifts compared to the WT. The action spectrum of WT-melanopsin (black) exhibits an action maximum (λ^{a}_{max}) of ~486 nm. The action spectrum of melanopsin-A333T (red) exhibited a λ^{a}_{max} of ~421 nm, while λ^{a}_{max} of A150L (blue), G153N (green), and Y309F/A333S (purple) were ~411, ~426 nm, and ~420 nm, respectively. **(d)** HeLa cells expressing blue opsin and mTq-Gγ9 exhibit rapidly attenuating Gγ9 translocation upon blue opsin activation in the presence of 50 nM 11CR ($n = 14$). In contrast, cells show sustained Gγ9 translocation upon blue light activation of lamprey parapinopsin (LPO) with 50 nM 11CR ($n = 12$). Grey arrows indicate the fluorescence intensity changes in the IMs due to Gγ9 translocation and attenuation. The whisker box plot shows the recovery extent of translocated Gγ9. **(e)** The attenuated Gγ9 translocation response with blue opsin in low retinal concentration (50 nM 11CR) can be rescued by increasing the retinal concentration up to 10 μM. Grey arrows indicate the changes in fluorescence intensity in the IMs. The corresponding line plot shows the mTq-Gγ9 dynamics in the IMs. The whisker box plot shows the attenuation extent of translocated Gγ9 with the two retinal concentrations. ($n = 8$) **(f)** The bistable melanopsin-WT exhibits non-attenuating, sustained Gγ9 translocation with blue light activation in the presence of 50 nM 11CR. Similarly, the mutants A333T, A150L, G153N, and Y309F/A333S exhibit sustained Gγ9 translocation upon blue light activation with 50 nM 11CR. The line plots show the mTq-Gγ9 dynamics in the IMs. The whisker box plot shows the recovery extent of translocated Gγ9 of WT ($n = 13$), A333T ($n = 11$), A150L ($n = 11$), G153N ($n = 10$), and Y309F/A333S ($n = 10$). Average curves were plotted using 'n' cells, n = number of cells. Error bars represent SD (standard deviation). Statistical comparisons were performed using one-way-ANOVA; $p<0.05$ (*: population means are significantly different)

added 10 μM 11CR to a Gγ9 translocation-attenuated cell in the presence of 50 nM 11CR (Fig. 11e, images of 10 s and 300 s), Gγ9 showed re-translocation (Fig. 11e, images at 420 s and 600 s). The Gγ9 translocation attenuation percentage with 50 nM 11CR was significantly higher than that with 10 μM 11CR (Fig. 11e, whisker plot, One-way ANOVA: $F_{1,15} = 174.93367$, $p=2.66E\text{-}9$, Table S8 a and b). These observations indicated that this assay could distinguish functional differences between monostable and bistable opsins. Nevertheless, this assay should be cautiously used, considering each of the stable state's signaling propensities and spectral properties.

Using the assay above, we examined sustained signaling under low 11CR of WT mMeOps and A333T, A150L,

G153N, and Y309F/A333S in HeLa cells also expressing mTq-Gγ9. When we exposed cells to blue light in the presence of 50 nM 11CR, WT mMeOps induced sustained Gγ9 translocation, further indicating the validity of this assay (Fig. 11f). A333T, A150L, G153N, and Y309F/A333S mutants also induced non-attenuating Gγ9 translocation responses upon blue light exposure (Fig. 11f). Like LPO, the calculated % recovery of Gγ9 translocation was negligible (Fig. 11f, whisker plot). This data indicated that the selected mutants showed sustained signaling under low retinal concentration, a finding indicating bistability.

A333T allows spatiotemporal control of single cells and subcellular G protein signaling

Since our data indicate that, unlike A150L, G153N, and Y309F/A333S, the A333T mutant has an increased Gq signaling activity with respect to WT mMeOps (Fig. 10b and Figure S8), we focus on such a mutant to probe its applicability in optogenetics. More specifically, we use A333T for temporal signaling control (using blue light) while continuously imaging cells (using red light). In fact, unlike WT mMeOp (Fig. 12a, images and plot), A333T expressing cells did not show PIP2 hydrolysis upon imaging mCh-PH (Fig. 12b, images up to 55 s, and plot's magenta background). However, robust PIP2 hydrolysis was detected after a 60 s long exposure of cells to both red and blue light (Fig. 12b, images of 90 s, and plot's blue background). This result indicated that by using A333T, one can capture pre- and post-stimulation signaling and cell behavior with a user-defined temporal control.

In previous works, we have shown cytoplasmic localized blue opsin activation and the resultant Gβγ-induced localized PIP3 and directional migration in live cells [34, 93]. However, unlike RAW264.7 macrophages and due to the lack of appropriate Gγ types, HeLa cells do not show PIP3 generation upon Gi/o GPCR activation [70]. Therefore, to examine melanopsin-induced localized PIP3 generation, we used RAW264.7 cells. RNAseq data shows that the endogenous Gαq level in RAW264.7 cells is significantly lower than other Gα subtypes [93]. Therefore, as described previously [93, 94], to increase Gβγ contribution from the Gq pathway, in addition to A333T or WT mMeOp and Akt-PH-mCh (PIP3 sensor), we also expressed Gαq-CFP in RAW264.7 cells. Next, in the presence of 10 μM 11CR, we exposed one side of the cell to blue light (Fig. 12c, image of 10 min: white box) while imaging Akt-PH-mCh using red light. Imaging WT mMeOp expressing cells using red light activated the opsin globally, inducing global PIP3 generation, which we did not observe for the mutant (Fig. 12c, white arrows, kymograph, and Supplementary Material 1 (movie S1)). Furthermore, localized blue light failed to induce subcellular signaling. In contrast, A333T activation induced localized PIP3 generation and migration of the cell towards the blue light (Fig. 12d, image of 10 min, yellow arrow, kymograph, and Supplementary Material 2 (movie S2)). Upon switching the blue light stimulus to the opposite side, the PIP3 generation was also switched (Fig. 12d, image of 24 min, white arrow, kymograph, and movie S2). This data demonstrates that similar to blue opsin, spectrally blue-shifted melanopsin variants such as A333T, can be used for spatiotemporal control of single-cell and subcellular signaling while imaging-based probing of resultant signaling and behavior using longer wavelengths.

Conclusions

In this work, we used a combined computational and experimental strategies to tackle a non-trivial problem in optogenetics: the engineering of novel bistable opsin mutants capable of being activated by wavelengths in the blue region while resisting activation under red light exposure. Ultimately, we have demonstrated that spectra of several predcited mutants, including the A333T mutant, are shifted towards the short wavelength region achieving the set goal. Consequently, we utilize A333T for subcellular G protein activation, localized PIP3 generation and directional cell migration, all monitored using red wavelength imaging.

The recently reported ARM protocol for building automatically (or semi-automatically) QM/MM models of rhodopsins and their mutants has been instrumental in the initial phase of the research, devoted to the prediction and selection of different short wavelength-shifted mMeOp mutants. This first phase has been followed by integrated computational and experimental studies searching for candidates that could not only have a short wavelength shifted absorption, but that could display an ultrafast isomerization reaction (and, thus, a possible high isomerization QY; one cause of the high light-sensitivity of melanopsins), only be activated by blue light, and maintain the bistability present in the WT form. A further selection has been based on biochemical essays targeting high signal production. We have also shown that the electrostatic rather than steric effect played the main role in inducing the short wavelength shifting effects on the opsin-embedded 11CR chromophore.

The studies above have been focused on ten blue-shifting mutations. However, live cell imaging showed that only six mutants resisted activation by red light without losing functionality when exposed to blue wavelengths. Ultimately, the A333T mutant was selected as the most promising candidate for the envisioned type of application. Indeed, A333T induces a significantly higher PIP2 hydrolysis under blue light exposure relative to WT mMeOp, indicating the signaling efficacy of the A333T mutant. Moreover, demonstrating the

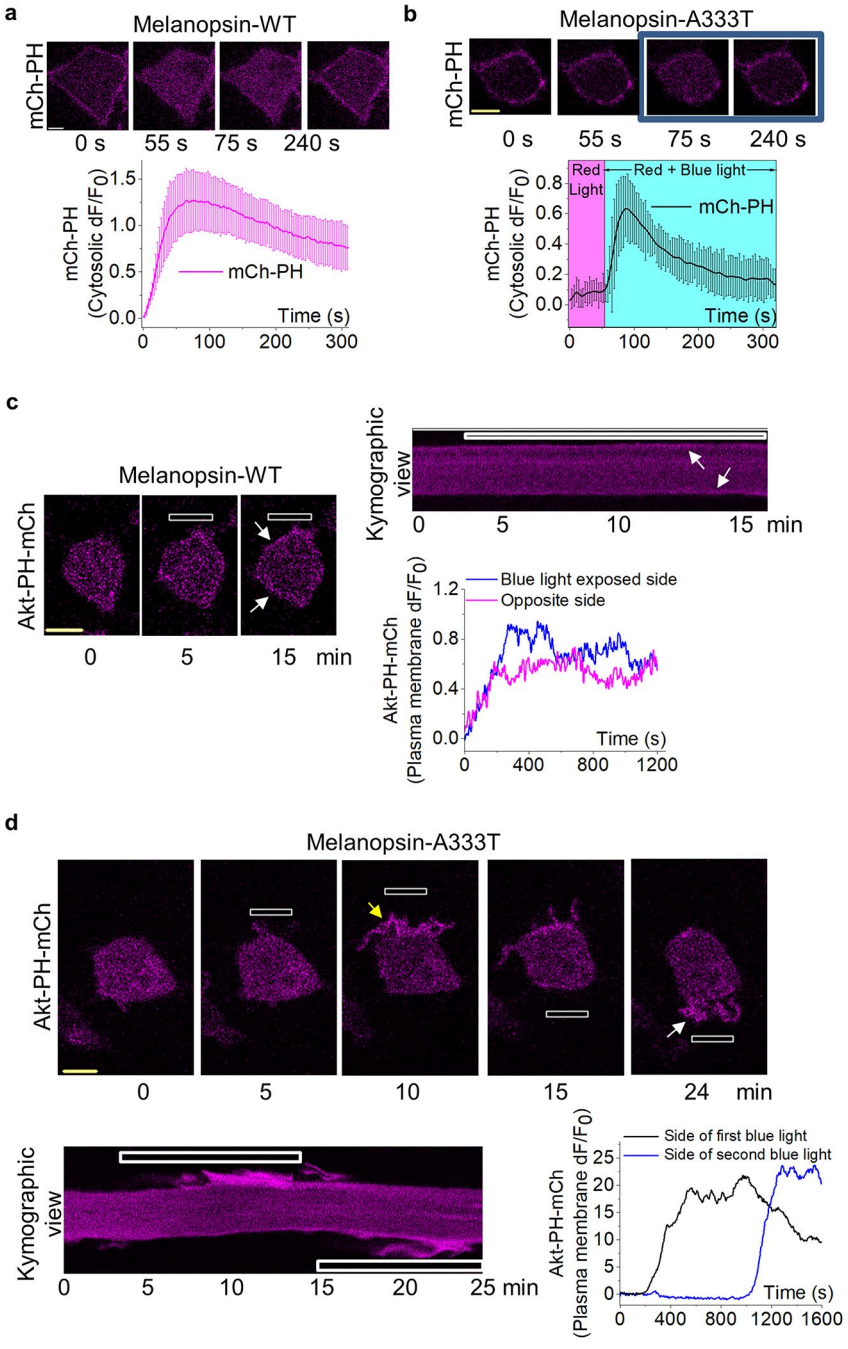

Fig. 12 Melanopsin-A333T mutant allows for spatio-temporal and subcellular G protein signaling control in living cells. **(a)** HeLa cells expressing melanopsin-WT and mCh-PH exhibit robust PIP2 hydrolysis upon red light illumination in the presence of 10 µM 11CR. The corresponding plot shows mCh-PH dynamics in the cytosol. ($n = 12$) **(b)** Melanopsin-A333T-expressing cells do not show a detectable PIP2 hydrolysis with red light; however, they exhibited robust PIP2 hydrolysis upon blue light exposure. The corresponding plot shows mCh-PH dynamics in the cytosol with red light (magenta background) and blue light (blue background) ($n = 10$). **(c)** RAW264.7 cells expressing melanopsin-WT and Akt-PH-mCh exhibit global PIP3 (white arrows) due to red light imaging despite localized blue light. The white box indicates the confined region of blue light. The corresponding plot shows Akt-PH-mCh dynamics on the PM. Although data is shown only from one cell, experiments were conducted in multiple cells to test the reproducibility. **(d)** RAW264.7 cells expressing melanopsin-A333T and Akt-PH-mCh exhibit localized PIP3 upon localized blue light activation (yellow arrows). Upon changing the blue light stimulus to the other side of the cell, PIP3 is generated from the blue light-exposed side (white arrows). The corresponding plot shows Akt-PH-mCh dynamics on the PM. The kymographic view of the cell indicates localized PIP3 generation with locally confined blue light. Although data is shown only from one cell, experiments were conducted in multiple cells to test the reproducibility. Average curves were plotted using 'n' cells, n = number of cells. Error bars represent SD (standard deviation)

subcellular signaling compatibility of the A333T mutant, we showed localized PIP3 generation and cell migration in macrophage cells using localized activation. In conclusion, as a proof-of-principle, we have demonstrated that a mMeOp mutant, designed with the help of QM/MM modeling, can be used to control subcellular signaling and will be a valuable optogenetic tool in dissecting crucial cell behaviors in physiology induced by spatially and temporally variable stimuli that are otherwise difficult to examine.

Methods

Reagents

The reagents used were as follows: Q5® Site-Directed Mutagenesis Kit (NEB), Gibson Assembly® Master Mix (NEB), and NEB® 5-alpha Competent E. coli (NEB), 11-*cis*-retinal (National Eye Institute), YM-254890 (Focus Biomolecules), Coelentrazine-H (AAT Bioquest), Pertussis toxin (Sigma-Aldrich). Stock solutions of compounds were prepared according to manufacturers' recommendations. Before being added to cells, all stock solutions were diluted in 1% Hank's balanced salt solution (HBSS) or a regular cell culture medium.

DNA constructs and cell lines

DNA constructs used were as follows: DNA constructs used for mCh-PH, GFP-PH, Venus-PH, Blue opsin-mTurquoise, and lamprey parapinopsin have been described previously [6, 67, 69, 96, 97]. Fluorescently tagged Gγ9 subunits and αq−CFP were kindly provided by Professor N. Gautam's laboratory, Washington University, St Louis, MO. mTq-PH was made by switching the mCherry fluorescent tag in mCh-PH (in PCDNA3.1) to mTurquoise using restriction cloning. All melanopsin mutants were created using site-directed mutagenesis (NEB) from the parent construct, melanopsin-1D4, in the PCDNA3.1 vector. All imaging and action spectra experiments were performed using melanopsin-WT and mutants in PCDNA3.1. For protein purification experiments, melanopsin-WT and mutants tagged with the rho-1D4 epitope sequence (ETSQVAPA) were inserted into the pMT vector using restriction cloning. Primers were designed using NEbuilder (for Gibson assembly or restriction cloning) and NEbasechanger (for site-directed mutagenesis). Cloned cDNA constructs were confirmed by sequencing from commercial sources. Cell lines used were as follows: HeLa and RAW264.7 cells were purchased from the American Tissue Culture Collection (ATCC).

Cell culture and transfections

HeLa cells were cultured in minimum essential medium (Corning) supplemented with 10% heat-inactivated dialyzed fetal bovine serum (DFBS, Atlanta Biologicals) and 1% penicillin-streptomycin-amphotericin (PSA, 100X stock, Corning) and grown at 37 °C with 5% CO_2. RAW264.7 cells were maintained in Roswell Park Memorial Institute (RPMI) 1640 medium (Corning) supplemented with 10% DFBS and 1% PSA. Cells were cultured in 35 mm, 60 mm, or 100 mm cell culture dishes (Celltreat). DNA transfections were performed using electroporation with the Cell line Nucleofector™ Kit V (RAW264.7 cells) or lipofectamine 2000 transfection reagent (HeLa cells) unless otherwise specified. For electroporation, the electroporation solution was prepared with the Nucleofector solution (82 µL), Supplement solution (18 µL), and appropriate volumes of DNA constructs. For each experiment, ~2–4 million cells were electroporated using the T020 method of the Nucleofector™ 2b device (Lonza). Immediately after electroporation, cells were mixed with cell culture medium at 37 ^{0}C and seeded onto 14 mm glass-bottomed wells (#1.5 glass coverslip) in 29 mm cell culture treated dishes. Cells were imaged ~5–6 h post-electroporation. Two days before imaging HeLa cells, 7×10^4 cells were seeded on a 14 mm glass bottom well with a #1.5 glass coverslip in a 29 mm cell culture dish. The following day, cells were transfected with appropriate DNA combinations using the transfection reagent Lipofectamine 2000 (Invitrogen) according to the manufacturer's protocol and then incubated in a 37 °C, 5% CO_2 incubator. Cells were imaged after 16 h of the transfection.

Live cell imaging, image analysis, and data processing

The methods, protocols, and parameters for live-cell imaging are adapted from published work [95, 98, 99]. Briefly, live-cell imaging, single-cell, and subcellular photo-stimulation experiments were performed using a spinning disk Confocal Imaging System (Yokogawa CSU-X1, 5000 rpm) composed of a Nikon Ti-R/B inverted microscope with a 60X, 1.4 NA oil objective and iXon ULTRA 897BVback-illuminated deep-cooled EMCCD camera. Photoactivation and Spatio-temporally controlled light exposure on cells in regions of interest (ROI) were performed using a laser combiner with 40–100 mW solid-state lasers (445, 488, 515, and 594 nm) equipped with Andor® FRAP-PA unit (fluorescence recovery after photobleaching and photoactivation), controlled by Andor iQ 3.1 software (Andor Technologies, Belfast, United Kingdom). Fluorescent sensors such as mCh-PH, mCh-γ9, and Akt-PH-mCh, were imaged using 594 nm excitation−624 nm emission settings; Venus-PH and Venus-γ9 were imaged using 515 nm excitation and 542 nm emission; GFP-PH and GFP-γ9 were imaged using 488 nm and 510 nm emission; mTq-PH, Gαq-CFP, Blue opsin-mTq was imaged using 445 nm excitation and 478 nm emission. In experiments with melanopsin, we imaged cells with the respective color to find cells with the sensor expression before adding retinal. Additional

adjustments of laser power with 0.1-1% transmittance were achieved using Acousto-optic tunable filters (AOTF). Ophir PD300-UV light meter was used for laser power measurements. Data acquisition, time-lapse image analysis, processing, and statistical analysis were performed as explained previously [95]. Briefly, Time-lapse images were analyzed using Andor iQ 3.1 software by acquiring the mean pixel fluorescence intensity changes of the entire cell or the selected area/regions of interest (ROIs). Briefly, the background intensity of images was subtracted from the intensities of the ROIs assigned to the desired areas of cells (plasma membrane, internal membranes, and cytosol) before intensity data collection from the time-lapse images. The intensity data from multiple cells were opened in Excel (Microsoft office®) and normalized to the baseline by dividing the data set by the average initial stable baseline value. Data were processed further using Origin-pro data analysis software (OriginLab®).

Aequorin reporter assay

HeLa cells at 75–85% confluency in a 100 mm dish were transfected with melanopsin (WT or mutants) alongside aequorin with PEI transfection reagent (in DNA: PEI, 1:1 mass ratio). On the next day, transfected cells were lifted and seeded on a 96-well, white-opaque tissue culture-grade plate with a density of 4×10^4 cells per well. The next day, action spectra for each melanopsin mutant and WT were obtained using the TECAN Spark advanced multimode microplate reader. Before luminescence measurements, 10 μM 11CR and 5 μM aequorin were added to the well and incubated for 3 min before the baseline luminescence was taken. Next, luminescence data were collected in response to different wavelengths of light (ranging from 230 to 650 nm). Each well was only exposed to one light wavelength. Luminescence data were collected and normalized to the baseline to calculate the luminescent fold increase in response to each wavelength. Our irradiance response data were fit using the validated, predicted absorbance spectrum for opsin: vitamin A-based photopigments from the Govardovskii template. [91] Data were further processed, and action spectra were plotted using the Origin-pro data analysis software (OriginLab®).

Expression and purification of melanopsin pigments and spectroscopy

Opsin expression and purification were performed as described previously [68]. Briefly, the full-length cDNAs expressing melanopsin-WT and mutants were tagged with the monoclonal antibody rho 1D4 epitope sequence (ETSQVAPA) and were inserted into the pMT vector. Opsin expression vectors were transfected into HEK293S cells using the calcium-phosphate method. 11CR (final concentration of 2.7 μM) was added to the culture medium 24 h after transfection and cultured in the dark for another 24 h, according to the previous report [30]. Cells were harvested 48 h post-transfection. The expressed proteins were incubated with an excess of 11CR overnight to reconstitute the pigment. Pigments were then extracted with 1% (w/v) dodecyl β-D-maltoside (DM) in HEPES buffer (pH 6.5) containing 140 mM NaCl and 3 mM $MgCl_2$, bound to 1D4-agarose, washed with 0.02% DM in the HEPES buffer and eluted with the HEPES buffer containing 0.02% DM and 1D4 peptide. The absorption spectra of the opsin-based pigments were recorded at 4 °C using the V-750 UV-VIS Spectrophotometer (JASCO International). Blue light (440 nm) was supplied using a light source with a 440 nm interference filter to obtain the light spectrum.

Computational methods

ARM protocol was used for the fast and automatic generation of combined (QM/MM) models of rhodopsin-like receptors as previously described [53, 64, 78] to predict opsin model absorption maxima as an average from the produced standard ten structural replicas. Briefly (see the cited references for details), the combination of the multi-configurational complete active space self-consistent field (CASSCF) [54, 78] method and the Amber force field is used to optimize the ground state geometries (single-root CASSCF(12,12)/6-31G*/Amber). The active space comprises the entire set of 12 electrons and 12 molecular orbitals describing the chromophore π-system). Excitation energies are then computed using multi-configurational second-order perturbation theory (CASPT2) [78], using a three-roots stage average (SA) CASSCF(12,12)/6-31G* wavefunction as a reference.

The structure of the ARM-generated QM/MM model is also described briefly. The model is divided into three subsystems: Environment, Cavity, and Lys-QM. The protein environment (treated at MM level) has a backbone and side-chain atoms fixed at the X-ray (or homology model) structure. The effect of the protein environment is indirectly incorporated with the introduction of counterions (Cl^- and/or Na^+), which generate a model with neutral inner and outer surfaces. The relaxed chromophore cavity (treated at MM level) has fixed backbone atoms, but its side-chain atoms are free to relax. It contains all the amino acid residues around the retinal chromophore. ARM uses the CASTp server (http://sts.bioe.uic.edu/castp/index.html ?2cpk) to obtain the list of cavity residues. The *Lys*-QM subsystem comprises the atoms of the lysine (though C_δ) to the entire retinal chromophore. All *Lys*-QM atoms are kept free to relax.

Statistical analysis

All experiments were repeated multiple times to test the reproducibility of the results. Statistical analysis and data plot generation were done using OriginPro software (OriginLab®). Results were analyzed from multiple cells on multiple days and represented as mean ± SD. The exact number of cells used in the analysis is given in respective figure legends. One-way ANOVA statistical tests were performed using OriginPro to determine the statistical significance between two or more populations of signaling responses. Tukey's mean comparison test was performed at the $p < 0.05$ significance level for the one-way ANOVA statistical test.

Abbreviations

11CR	11-*cis*-retinal
ARM	Automatic rhodopsin modeling
ATR	All-*trans*-retinal
BO	Blue opsin
CoIn	Conical intersection
DAG	Diacylglycerol
Ea	Photoactivation energy
ECL	Extracellular loop
FC	Franck-condon
GPCR	G protein-coupled receptor
hMeOp	Human melanopsin
IP3	Inositol triphosphate
ipRGCs	Intrinsically photosensitive retinal ganglion cells
LPO	Lamprey parapinopsin
mMeOp	Mouse melanopsin
PIP2	Phosphatidylinositol 4,5-bisphosphate
PIP3	Phosphatidylinositol (3,4,5)-trisphosphate
PLCβ	Phospholipase Cβ
PSB	Protonated Schiff base
Ptx	Pertussis toxin
QM/MM	Quantum mechanical/molecular mechanical
QY	Quantum yield
RMSD	Root mean squared deviation
S_0	Electronic ground state
S_1	First Excited state
S_2	Second excited state
SBN	Schiff base nitrogen
SCN	Suprachiasmatic nucleus
SqRh	Squid rhodopsin
SW1	Short wavelength-sensitive type 1
TM	Transmembrane
WT	Wild-type
λ'_{max}	Red shifted maximum absorption wavelength
λ''_{max}	Blue shifted maximum absorption wavelength
λ^{a}_{max}	Maximum absorption wavelength

Supplementary Information

The online version contains supplementary material available at https://doi.org/10.1186/s12964-024-01753-0.

Supplementary Material 1

Supplementary Material 2

Supplementary Material 3

Acknowledgements

We acknowledge Dr. N. Gautam for providing us with plasmid DNA of various G protein subunits and for the RNA seq data. We thank the National Eye Institute for providing 11-*cis*-retinal. We thank Robert S. Molday (University of British Columbia) for supplying rho 1D4-producing hybridoma. We also thank Dinesh Kankanamge for their experimental assistance.

Author contributions

D. W. And F.S. contributed equally to the study. D.W. conducted the action spectra, the majority of live cell imaging experiments, and the data analysis. F.S. performed all the computational analyses using the Modeller and ARM. L.P.G. developed the ARM protocol, and F.F. generated the melanopsin homology model. M.K. T.S. and A.T. conducted the melanopsin pigment purification and spectroscopic studies. S.P. conducted the Gγ9 translocation experiments and assisted in data analysis. K.G. performed the control experiments for the live cell imaging assay for bistability. W.T. made the mTq-PH construct. A.K., D.W., and M.O. conceptualized the project and wrote the manuscript.

Funding

The work was funded by a grant from the National Institutes of Health (NIH)- National Institute of General Medical Sciences (NIGMS) (Grant number: 1R01GM140191-01). M. O. is grateful for partial support provided by EU funding within the MUR PNRR "National Center for Gene Therapy and Drugs based on RNA Technology" (Project no. CN00000041 CN3 RNA) - Spoke 6. M. O. is also grateful to the NSF CHE-SDM A for Grant No. 2102619.

Data availability

No datasets were generated or analysed during the current study.

Declarations

Competing interests

The authors declare no competing interests.

Received: 12 March 2024 / Accepted: 17 July 2024
Published online: 08 August 2024

References

1. Deisseroth K, Feng G, Majewska AK, Miesenbock G, Ting A, Schnitzer MJ. Next-generation optical technologies for illuminating genetically targeted brain circuits. J Neurosci. 2006;26(41):10380–6. https://doi.org/10.1523/JNEUROSCI.3863-06.2006PubMed.
2. Fenno L, Yizhar O, Deisseroth K. The Development and Application of optogenetics. Annu Rev Neurosci. 2011;34(1):389–412. https://doi.org/10.1146/annurev-neuro-061010-113817.
3. Gradinaru V, Zhang F, Ramakrishnan C, Mattis J, Prakash R, Diester I, Goshen I, Thompson KR, Deisseroth K. Molecular and Cellular approaches for Diversifying and extending optogenetics. Cell. 2010;141(1):154–65. https://doi.org/10.1016/j.cell.2010.02.037. (acccessed 2023/09/26).
4. Kim CK, Adhikari A, Deisseroth K. Integration of optogenetics with complementary methodologies in systems neuroscience. Nat Rev Neurosci. 2017;18(4):222–35. https://doi.org/10.1038/nrn.2017.15.
5. Montgomery KL, Yeh AJ, Ho JS, Tsao V, Mohan Iyer S, Grosenick L, Ferenczi EA, Tanabe Y, Deisseroth K, Delp SL, Poon AS. Y. wirelessly powered, fully internal optogenetics for brain, spinal and peripheral circuits in mice. Nat Methods. 2015;12(10):969–74. https://doi.org/10.1038/nmeth.3536.
6. Karunarathne WKA, Giri L, Kalyanaraman V, Gautam N. Optically triggering spatiotemporally confined GPCR activity in a cell and programming neurite initiation and extension. Proc Natl Acad Sci U S A. 2013;110(17):E1565–74.
7. Koyanagi M, Saito T, Wada S, Nagata T, Kawano-Yamashita E, Terakita A. Optogenetic potentials of Diverse Animal opsins: Parapinopsin, Peropsin, LWS Bistable opsin. In: Yawo H, Kandori H, Koizumi A, Kageyama R, editors. Optogenetics: light-sensing proteins and their applications in Neuroscience and Beyond. Eds.; Springer Singapore,; 2021. pp. 141–51.
8. Eickelbeck D, Rudack T, Tennigkeit SA, Surdin T, Karapinar R, Schwitalla JC, Mucher B, Shulman M, Scherlo M, Althoff P, et al. Lamprey Parapinopsin (UVLamP): a bistable UV-Sensitive optogenetic switch for Ultrafast Control of GPCR pathways. ChemBioChem. 2020;21(5):612–7. https://doi.org/10.1002/cbic.201900485.
9. Koyanagi M, Terakita A. Diversity of animal opsin-based pigments and their optogenetic potential. Biochim Biophys Acta. 2014;1837(5):710–6. https://doi.org/10.1016/j.bbabio.2013.09.003.

10. Hagio H, Koyama W, Hosaka S, Song AD, Narantsatsral J, Matsuda K, Sugihara T, Shimizu T, Koyanagi M, Terakita A, Hibi M. Optogenetic manipulation of Gq- and Gi/o-coupled receptor signaling in neurons and heart muscle cells. eLife. 2023;12:e83974. https://doi.org/10.7554/eLife.83974.
11. Palczewski K, Kumasaka T, Hori T, Behnke CA, Motoshima H, Fox BA, Le Trong I, Teller DC, Okada T, Stenkamp RE, et al. Crystal structure of rhodopsin: a G protein-coupled receptor. Science. 2000;289(5480):739–45. https://doi.org/10.1126/science.289.5480.739. From NLM.
12. Okada T, Ernst OP, Palczewski K, Hofmann KP. Activation of rhodopsin: new insights from structural and biochemical studies. Trends Biochem Sci. 2001;26(5):318–24. https://doi.org/10.1016/s0968-0004(01)01799-6. From NLM.
13. Tsukamoto H, Terakita A. Diversity and functional properties of bistable pigments. Photochem Photobiol Sci. 2010;9(11):1435–43. https://doi.org/10.1039/C0PP00168F.
14. Sakmar TP, Franke RR, Khorana HG. Glutamic acid-113 serves as the retinylidene Schiff base counterion in bovine rhodopsin. Proc Natl Acad Sci U S A. 1989;86(21):8309–13. https://doi.org/10.1073/pnas.86.21.8309. From NLM.
15. Sakmar TP, Franke RR, Khorana HG. The role of the retinylidene Schiff base counterion in rhodopsin in determining wavelength absorbance and Schiff base pKa. Proc Natl Acad Sci U S A. 1991;88(8):3079–83.
16. Kimata N, Pope A, Eilers M, Opefi CA, Ziliox M, Hirshfeld A, Zaitseva E, Vogel R, Sheves M, Reeves PJ. Retinal orientation and interactions in rhodopsin reveal a two-stage trigger mechanism for activation. Nat Commun. 2016;7(1):12683.
17. Murakami M, Kouyama T. Crystal structure of squid rhodopsin. Nature. 2008;453(7193):363–7. https://doi.org/10.1038/nature06925.
18. Varma N, Mutt E, Mühle J, Panneels V, Terakita A, Deupi X, Nogly P, Schertler GFX, Lesca E. Crystal structure of jumping spider rhodopsin-1 as a light sensitive GPCR. Proc Natl Acad Sci USA. 2019;116(29):14547–56. https://doi.org/10.1073/pnas.1902192116.
19. Contreras E, Nobleman AP, Robinson PR, Schmidt TM. Melanopsin phototransduction: beyond canonical cascades. J Exp Biol. 2021;224(23). https://doi.org/10.1242/jeb.226522. (acccessed 5/22/2024).
20. Li G, Chen L, Jiang Z, Yau K-W. Coexistence within one cell of microvillous and ciliary phototransductions across M1- through M6-IpRGCs. Proc Natl Acad Sci. 2023;120(52):e2315282120. https://doi.org/10.1073/pnas.2315282120.
21. Beaulé C, Robinson B, Lamont EW, Amir S. Melanopsin in the circadian timing system. J Mol Neurosci. 2003;21(1):73–89. https://doi.org/10.1385/jmn:21:1.:73 From NLM.
22. Gillette MU, Tischkau SA. Suprachiasmatic nucleus: the brain's circadian clock. Recent Prog Horm Res. 1999;54:33–58. discussion 58 – 39. From NLM.
23. Schmidt TM, Chen SK, Hattar S. Intrinsically photosensitive retinal ganglion cells: many subtypes, diverse functions. Trends Neurosci. 2011;34(11):572–80. https://doi.org/10.1016/j.tins.2011.07.001. From NLM.
24. Walker WH 2nd;, Walton JC, DeVries AC, Nelson RJ. Circadian rhythm disruption and mental health. Transl Psychiatry. 2020;10(1):28. https://doi.org/10.1038/s41398-020-0694-0. From NLM.
25. Terakita A, Tsukamoto H, Koyanagi M, Sugahara M, Yamashita T, Shichida Y. Expression and comparative characterization of Gq-coupled invertebrate visual pigments and melanopsin. J Neurochem. 2008;105(3):883–90. https://doi.org/10.1111/j.1471-4159.2007.05184.x.
26. Qiu X, Kumbalasiri T, Carlson SM, Wong KY, Krishna V, Provencio I, Berson DM. Induction of photosensitivity by heterologous expression of melanopsin. Nature. 2005;433(7027):745–9. https://doi.org/10.1038/nature03345.
27. Bailes HJ, Lucas RJ. Human melanopsin forms a pigment maximally sensitive to blue light (λmax ≈ 479 nm) supporting activation of G(q/11) and G(i/o) signalling cascades. Proc Biol Sci. 2013;280(1759):20122987. https://doi.org/10.1098/rspb.2012.2987. From NLM.
28. Kankanamge D, Ratnayake K, Samaradivakara S, Karunarathne A, Melanopsin. (Opn4) utilizes Gα(i) and Gβγ as major signal transducers. J Cell Sci. 2018;131(11). https://doi.org/10.1242/jcs.212910. From NLM.
29. McDowell RJ, Rodgers J, Milosavljevic N, Lucas RJ. Divergent G-protein selectivity across melanopsins from mice and humans. J Cell Sci. 2022;135(6). https://doi.org/10.1242/jcs.258474. (acccessed 9/23/2023).
30. Matsuyama T, Yamashita T, Imamoto Y, Shichida Y. Photochemical properties of mammalian melanopsin. Biochemistry. 2012;51(27):5454–62. https://doi.org/10.1021/bi3004999. From NLM.
31. El-Tahawy MMT, Nenov A, Weingart O, Olivucci M, Garavelli M. Relationship between Excited State Lifetime and Isomerization Quantum yield in animal rhodopsins: beyond the one-Dimensional Landau-Zener Model. J Phys Chem Lett. 2018;9 12:3315–22.
32. Enezi Ja, Revell V, Brown T, Wynne J, Schlangen L, Lucas RA. Melanopic spectral efficiency function predicts the sensitivity of Melanopsin photoreceptors to polychromatic lights. J Biol Rhythm. 2011;26(4):314–23. 10.1177/0748730411409719 From NLM.
33. Karunarathne WKA, Giri L, Patel AK, Venkatesh KV, Gautam N. Optical control demonstrates switch-like PIP3 dynamics underlying the initiation of immune cell migration. Proc Natl Acad Sci U S A. 2013;110(17):E1575–83. https://doi.org/10.1073/pnas.1220755110.
34. Siripurapu P, Kankanamge D, Ratnayake K, Senarath K, Karunarathne A. Two independent but synchronized Gbetagamma subunit-controlled pathways are essential for trailing-edge retraction during macrophage migration. J Biol Chem. 2017;292(42):17482–95. https://doi.org/10.1074/jbc.M117.787838. (acccessed 2022/04/04).
35. Altun A, Yokoyama S, Morokuma K. Spectral tuning in visual pigments: an ONIOM(QM:MM) study on bovine rhodopsin and its mutants. J Phys Chem B. 2008;112(22):6814–27. https://doi.org/10.1021/jp709730b. From NLM.
36. Yokoyama R, Yokoyama S. Convergent evolution of the red- and green-like visual pigment genes in fish, Astyanax fasciatus, and human. Proc Natl Acad Sci U S A. 1990;87(23):9315–8. https://doi.org/10.1073/pnas.87.23.9315. From NLM.
37. Rajamani R, Lin YL, Gao J. The opsin shift and mechanism of spectral tuning in rhodopsin. J Comput Chem. 2011;32(5):854–65. https://doi.org/10.1002/jcc.21663. From NLM.
38. Saito T, Koyanagi M, Sugihara T, Nagata T, Arikawa K, Terakita A. Spectral tuning mediated by helix III in butterfly long wavelength-sensitive visual opsins revealed by heterologous action spectroscopy. Zoological Lett. 2019;5(1):35. https://doi.org/10.1186/s40851-019-0150-2.
39. Musilova Z, Salzburger W, Cortesi F. The visual opsin gene repertoires of Teleost fishes: Evolution, Ecology, and function. Annu Rev Cell Dev Biol. 2021;37:441–68. https://doi.org/10.1146/annurev-cellbio-120219-024915. From NLM.
40. Marshall J, Carleton KL, Cronin T. Colour vision in marine organisms. Curr Opin Neurobiol. 2015;34:86–94. https://doi.org/10.1016/j.conb.2015.02.002.
41. Cronin TW, Hariyama T. Spectral sensitivity in Crustacean eyes. Berlin, Heidelberg: Springer Berlin Heidelberg; 2002. pp. 499–511.
42. Liénard MA, Valencia-Montoya WA, Pierce NE. Molecular advances to study the function, evolution and spectral tuning of arthropod visual opsins. Philosophical Trans Royal Soc B: Biol Sci. 2022;377(1862):20210279. https://doi.org/10.1098/rstb.2021.0279.
43. Donner K, Zak P, Viljanen M, Lindström M, Feldman T, Ostrovsky M. Eye spectral sensitivity in fresh- and brackish-water populations of three glacial-relict Mysis species (Crustacea): physiology and genetics of differential tuning. J Comp Physiol A. 2016;202(4):297–312. https://doi.org/10.1007/s00359-016-1079-y.
44. Hunt DM, Dulai KS, Partridge JC, Cottrill P, Bowmaker JK. The molecular basis for spectral tuning of rod visual pigments in deep-sea fish. J Exp Biol. 2001;204(19):3333–44. https://doi.org/10.1242/jeb.204.19.3333. (acccessed 5/23/2024).
45. Wilkie SE, Robinson PR, Cronin TW, Poopalasundaram S, Bowmaker JK, Hunt DM. Spectral tuning of Avian Violet- and Ultraviolet-Sensitive Visual pigments. Biochemistry. 2000;39(27):7895–901. https://doi.org/10.1021/bi992776m.
46. Hauser FE, Chang BS. Insights into visual pigment adaptation and diversity from model ecological and evolutionary systems. Curr Opin Genet Dev. 2017;47:110–20. https://doi.org/10.1016/j.gde.2017.09.005. From NLM.
47. Gai Y, Tian R, Liu F, Mu Y, Shan L, Irwin DM, Liu Y, Xu S, Yang G. Diversified mammalian visuasl adaptations to Bright- or dim-light environments. Mol Biol Evol. 2023;40(4). https://doi.org/10.1093/molbev/msad063.
48. Borges R, Johnson WE, O'Brien SJ, Gomes C, Heesy CP, Antunes A. Adaptive genomic evolution of opsins reveals that early mammals flourished in nocturnal environments. BMC Genomics. 2018;19(1):121. https://doi.org/10.1186/s12864-017-4417-8. From NLM.
49. Chan T, Lee M, Sakmar TP. Introduction of hydroxyl-bearing amino acids causes bathochromic spectral shifts in rhodopsin. Amino acid substitutions responsible for red-green color pigment spectral tuning. J Biol Chem. 1992;267(14):9478–80. https://doi.org/10.1016/S0021-9258(19)50115-6.
50. Hunt DM, Carvalho LS, Cowing JA, Parry JWL, Wilkie SE, Davies WL, Bowmaker JK. Spectral tuning of Shortwave-sensitive visual pigments in Vertebrates†. Photochem Photobiol. 2007;83(2):303–10. https://doi.org/10.1562/2006-06-27-IR-952.
51. Kleinschmidt J, Harosi FI. Anion sensitivity and spectral tuning of cone visual pigments in situ. Proc Natl Acad Sci U S A. 1992;89(19):9181–5. https://doi.org/10.1073/pnas.89.19.9181.

52. Warshel A. Bicycle-pedal model for the first step in the vision process. Nature. 1976;260(5553):679–83. https://doi.org/10.1038/260679a0.
53. Pedraza-González L, De Vico L, Marín F, Olivucci M. a-ARM: Automatic Rhodopsin Modeling with Chromophore Cavity Generation, Ionization State Selection, and External Counterion Placement. *Journal of Chemical Theory and Computation* 2019, *15* (5), 3134–3152. https://doi.org/10.1021/acs.jctc.9b00061.
54. Gozem S, Luk HL, Schapiro I, Olivucci M. Theory and Simulation of the Ultrafast Double-Bond Isomerization of Biological Chromophores. *Chemical Reviews* 2017, *117* (22), Medium: X; Size: 13502 to 13565.
55. Pahlberg J, Lindström M, Ala-Laurila P, Fyhrquist-Vanni N, Koskelainen A, Donner K. The photoactivation energy of the visual pigment in two spectrally different populations of Mysis relicta (Crustacea, Mysida). J Comp Physiol A. 2005;191(9):837–44. https://doi.org/10.1007/s00359-005-0005-5.
56. Koskelainen A, Ala-Laurila P, Fyhrquist N, Donner K. Measurement of thermal contribution to photoreceptor sensitivity. Nature. 2000;403(6766):220–3. https://doi.org/10.1038/35003242.
57. Stiles W. Transactions of the Optical Convention of the Worshipful Company of Spectacle Makers. 1948.
58. Barlow H. Purkinje shift and retinal noise. Nature. 1957;179(4553):255–6.
59. Firsov M, Govardovskii V. Dark noise of visual pigments with different absorption maxima. Sens Syst. 1990;4(1):25–34.
60. Ala-Laurila P, Saarinen P, Albert R, Koskelainen A, Donner K. Temperature effects on spectral properties of red and green rods in toad retina. Vis Neurosci. 2002;19(6):781–92.
61. Ala-Laurila P, Albert R-J, Saarinen P, Koskelainen A, Donner K. The thermal contribution to photoactivation in A2 visual pigments studied by temperature effects on spectral properties. Vis Neurosci. 2003;20(4):411–9.
62. Rieke F, Baylor DA. Origin and functional impact of dark noise in retinal cones. Neuron. 2000;26(1):181–6.
63. Ala–Laurila P, Estevez M, Crouch RK, Wiggert B, Cornwall MC. Production and clearance of all–trans Retinol in bleached rods and cones depend on opsin type and photoreceptor morphology. Investig Ophthalmol Vis Sci. 2005;46(13):3968–3968. (acccessed 6/17/2024).
64. Pedraza-González L, Barneschi L, Marszałek M, Padula D, De Vico L, Olivucci M. Automated QM/MM screening of rhodopsin variants with enhanced fluorescence. J Chem Theory Comput. 2023;19(1):293–310. https://doi.org/10.1021/acs.jctc.2c00928. From NLM.
65. Matsuyama T, Yamashita T, Imamoto Y, Shichida Y. Photochemical properties of mammalian Melanopsin. Biochemistry. 2012;51(27):5454–62. https://doi.org/10.1021/bi3004999.
66. Newman LA, Walker MT, Brown RL, Cronin TW, Robinson PR. Melanopsin forms a functional short-wavelength photopigment. Biochemistry. 2003;42(44):12734–8. https://doi.org/10.1021/bi035418z.
67. Koyanagi M, Kawano E, Kinugawa Y, Oishi T, Shichida Y, Tamotsu S, Terakita A. Bistable UV pigment in the lamprey pineal. Proc Natl Acad Sci U S A. 2004;101(17):6687. https://doi.org/10.1073/pnas.0400819101.
68. Koyanagi M, Takada E, Nagata T, Tsukamoto H, Terakita A. Homologs of vertebrate Opn3 potentially serve as a light sensor in nonphotoreceptive tissue. Proc Natl Acad Sci U S A. 2013;110(13):4998–5003. https://doi.org/10.1073/pnas.1219416110. From NLM.
69. Kankanamge D, Ubeysinghe S, Tennakoon M, Pantula P.D., Mitra K, Giri L, Karunarathne A. Dissociation of the G protein betagamma from the Gq-PLCbeta complex partially attenuates PIP2 hydrolysis. J Biol Chem. 2021;296. https://doi.org/10.1016/j.jbc.2021.100702. acccessed 2022/01/12.
70. Senarath K, Payton JL, Kankanamge D, Siripurapu P, Tennakoon M, Karunarathne A. Gγ identity dictates efficacy of Gβγ signaling and macrophage migration. J Biol Chem. 2018;293(8):2974–89. https://doi.org/10.1074/jbc.RA117.000872.
71. Tennakoon M, Senarath K, Kankanamge D, Ratnayake K, Wijayaratna D, Olupothage K, Ubeysinghe S, Martins-Cannavino K, Hébert TE, Karunarathne A. Subtype-dependent regulation of Gβγ signalling. Cell Signal 2021, 109947.
72. Taniguchi M, Suzumura K-i, Nagai K, Kawasaki T, Saito T, Takasaki J, Suzuki K-i, Fujita S, Tsukamoto S. -i. structure of YM-254890, a novel Gq/11 inhibitor from Chromobacterium sp. QS3666. Tetrahedron. 2003;59(25):4533–8. https://doi.org/10.1016/S0040-4020(03)00680-X.
73. Srinivasan S, Fernández-Sampedro MA, Morillo M, Ramon E, Jiménez-Rosés M, Cordomí A, Garriga P. Human Blue Cone Opsin Regeneration Involves Secondary Retinal Binding with Analog specificity. Biophys J. 2018;114(6):1285–94. https://doi.org/10.1016/j.bpj.2018.01.032. From NLM.
74. Saito T, Koyanagi M, Sugihara T, Nagata T, Arikawa K, Terakita A. Spectral tuning mediated by helix III in butterfly long wavelength-sensitive visual opsins revealed by heterologous action spectroscopy. Zoological Lett. 2019;5:35. https://doi.org/10.1186/s40851-019-0150-2. From NLM.
75. Liénard MA, Valencia-Montoya WA, Pierce NE. Molecular advances to study the function, evolution and spectral tuning of arthropod visual opsins. Philos Trans R Soc Lond B Biol Sci. 2022;377(1862):20210279. https://doi.org/10.1098/rstb.2021.0279. From NLM.
76. Webb B, Sali A. Comparative protein structure modeling using MODELLER. Curr Protoc Bioinf. 2016;54:561–5637. https://doi.org/10.1002/cpbi.3. From NLM.
77. MacKerell AD Jr., Banavali N, Foloppe N. Development and current status of the CHARMM force field for nucleic acids. Biopolymers. 2000;56(4):257–65. https://doi.org/10.1002/1097-0282(2000)56:4<257::Aid-bip10029>3.0.Co;2.
78. Melaccio F, Del Carmen Marín M, Valentini A, Montisci F, Rinaldi S, Cherubini M, Yang X, Kato Y, Stenrup M, Orozco-Gonzalez Y, et al. Toward automatic rhodopsin modeling as a Tool for High-Throughput Computational Photobiology. J Chem Theory Comput. 2016;12(12):6020–34. https://doi.org/10.1021/acs.jctc.6b00367. From NLM.
79. Nakajima Y, Pedraza-González L, Barneschi L, Inoue K, Olivucci M, Kandori H. Pro219 is an electrostatic color determinant in the light-driven sodium pump KR2. Commun Biology. 2021;4(1):1185. https://doi.org/10.1038/s42003-021-02684-z.
80. Pedraza-González L, Barneschi L, Padula D, De Vico L, Olivucci M. Evolution of the Automatic Rhodopsin Modeling (ARM) Protocol. *Topics in Current Chemistry (Cham)* 2022, *380*.
81. Yabushita A, Kobayashi T, Tsuda M. Time-resolved spectroscopy of ultrafast photoisomerization of octopus rhodopsin under photoexcitation. J Phys Chem B. 2012;116(6):1920–6. https://doi.org/10.1021/jp209356s. From NLM.
82. Rinaldi S, Melaccio F, Gozem S, Fanelli F, Olivucci M. Comparison of the isomerization mechanisms of human melanopsin and invertebrate and vertebrate rhodopsins. Proc Natl Acad Sci U S A. 2014;111(5):1714–9. https://doi.org/10.1073/pnas.1309508111.
83. Gozem S, Huntress M, Schapiro I, Lindh R, Granovsky AA, Angeli C, Olivucci M. Dynamic electron correlation effects on the ground state potential energy surface of a retinal chromophore model. *Journal of Chemical Theory and Computation* 2012, *8* (11), 4069–4080, Article. https://doi.org/10.1021/ct3003139.
84. Yang X, Manathunga M, Gozem S, Léonard J, Andruniów T, Olivucci M. Quantum-classical simulations of rhodopsin reveal excited-state population splitting and its effects on quantum efficiency. Nat Chem. 2022;14(4):441–9. https://doi.org/10.1038/s41557-022-00892-6. From NLM.
85. Gozem S, Schapiro I, Ferré N, Olivucci M. The molecular mechanism of thermal noise in rod photoreceptors. Science. 2012;337(6099):1225–8. https://doi.org/10.1126/science.1220461. From NLM.
86. Zhu GY, Qin Y, Meng M, Mallick S, Gao H, Chen X, Cheng T, Tan YN, Xiao X, Han MJ, et al. Crossover between the adiabatic and nonadiabatic electron transfer limits in the Landau-Zener model. Nat Commun. 2021;12(1):456. https://doi.org/10.1038/s41467-020-20557-7.
87. Boeije Y, Olivucci M. From a one-mode to a multi-mode understanding of conical intersection mediated ultrafast organic photochemical reactions. Chem Soc Rev. 2023;52(8):2643–87. https://doi.org/10.1039/D2CS00719C.
88. Kankanamge D, Ratnayake K, Samaradivakara S, Karunarathne A. Melanopsin (Opn4) utilizes Gαiand Gβγ as major signal transducers. J Cell Sci. 2018;131(11). https://doi.org/10.1242/jcs.212910.
89. Bailes HJ, Lucas RJ. Human melanopsin forms a pigment maximally sensitive to blue light (λmax≈479 nm) supporting activation of G(q/11) and G(i/o) signalling cascades. Proc Royal Soc B. 2013;280(1759):20122987. https://doi.org/10.1098/rspb.2012.2987.
90. Shimomura O, Musicki B, Kishi Y, Inouye yS. Light-emitting properties of recombinant semisynthetic aequorins and recombinant fluorescein-conjugated aequorin for measuring cellular calcium. Cell Calcium. 1993;14(5):373–8.
91. Govardovskii VI, Fyhrquist N, Reuter T, Kuzmin DG, Donner K. In search of the visual pigment template. Vis Neurosci. 2000;17(4):509–28.
92. Ehrenberg D, Varma N, Deupi X, Koyanagi M, Terakita A, Schertler GFX, Heberle J, Lesca E. The two-photon reversible reaction of the Bistable jumping spider Rhodopsin-1. Biophys J. 2019;116(7):1248–58. https://doi.org/10.1016/j.bpj.2019.02.025. From NLM.
93. Wijayaratna D, Ratnayake K, Ubeysinghe S, Kankanamge D, Tennakoon M, Karunarathne A. The spatial distribution of GPCR and Gβγ activity across a cell dictates PIP3 dynamics. Sci Rep. 2023;13(1):2771. https://doi.org/10.1038/s41598-023-29639-0.
94. Kankanamge D, Tennakoon M, Weerasinghe A, Cedeno-Rosario L, Chadee DN, Karunarathne. A. G protein alphaq exerts expression level-dependent

distinct signaling paradigms. Cell Signal. 2019;58:34–43. https://doi.org/10.1016/j.cellsig.2019.02.006.
95. Ratnayake K, Payton JL, Lakmal OH, Karunarathne A. Blue light excited retinal intercepts cellular signaling. Sci Rep. 2018;8(1):10207. https://doi.org/10.1038/s41598-018-28254-8.
96. Chisari M, Saini DK, Cho J-H, Kalyanaraman V. Gautam, N. G protein subunit dissociation and translocation regulate cellular response to receptor stimulation. PLoS ONE 2009, 4 (11), e7797.
97. O'Neill PR, Kalyanaraman V, Gautam N. Subcellular optogenetic activation of Cdc42 controls local and distal signaling to drive immune cell migration. Mol Biol Cell. 2016;27(9):1442–50.
98. Ratnayake K, Payton JL, Meger ME, Godage NH, Gionfriddo E, Karunarathne A. Blue light-triggered photochemistry and cytotoxicity of retinal. Cell Signal. 2020;109547. https://doi.org/10.1016/j.cellsig.2020.109547.
99. Senarath K, Ratnayake K, Siripurapu P, Payton JL, Karunarathne A, Reversible G. Protein betagamma9 distribution-based assay reveals molecular underpinnings in Subcellular, Single-Cell, and multicellular GPCR and G protein activity. Anal Chem. 2016;88(23):11450–9. https://doi.org/10.1021/acs.analchem.6b02512.

Publisher's Note